Probing a Single Isolated Electron:
New Measurements of the Electron Magnetic Moment
and the Fine Structure Constant

Gerald GABRIELSE
Leverett Professor of Physics
Harvard University
Cambridge, MA 02138

1 Introduction

For these measurements one electron is suspended for months at a time within a cylindrical Penning trap [1], a device that was invented long ago just for this purpose. The cylindrical Penning trap provides an electrostatic quadrupole potential for trapping and detecting a single electron [2]. At the same time, it provides a right, circular microwave cavity that controls the radiation field and density of states for the electron's cyclotron motion [3].

Quantum jumps between Fock states of the one-electron cyclotron oscillator reveal the quantum limit of a cyclotron [4]. With a surrounding cavity inhibiting synchrotron radiation 140-fold, the jumps show as long as a 13 s Fock state lifetime, and a cyclotron in thermal equilibrium with 1.6 to 4.2 K blackbody photons. These disappear by 80 mK, a temperature 50 times lower than previously achieved with an isolated elementary particle. The cyclotron stays in its ground state until a resonant photon is injected. A quantum cyclotron offers a new route to measuring the electron magnetic moment and the fine structure constant.

The use of electronic feedback is a key element in working with the one-electron quantum cyclotron. A one-electron oscillator is cooled from 5.2 K to 850 mK using electronic feedback [5]. Novel quantum jump thermometry reveals a Boltzmann distribution of oscillator energies and directly measures the corresponding temperature. The ratio of electron temperature and damping rate (also directly measured) is observed to be a fluctuation-dissipation invariant, independent of feedback gain, as predicted for noiseless feedback. The sharply reduced linewidth that results from feedback cooling illustrates the likely importance for improved fundamental measurements and symmetry tests.

Electronic feedback that self-excites the axial oscillation of a single electron in a Penning trap is used to detect spin flips and one-quantum cyclotron excitations [6]. Large, stable, easily detected oscillations arise even in an anharmonic potential. Amplitudes are controlled by adjusting the feedback gain, and frequencies can be made nearly independent of amplitude fluctuations. Quantum jump spectroscopy of a perpendicular cyclotron motion reveals the absolute temperature and amplitude of the self-excited oscillation. The possibility to quickly measure ppb frequency shifts opens the way to improved measurements of the electron magnetic moment.

The new experimental methods make it possible for the first time to use quantum jump spectroscopy of the lowest cyclotron and spin levels for a single-electron

quantum cyclotron [7]. The measured electron magnetic moment has an uncertainty that is nearly six times lower than in the past, and the moment is shifted downward by 1.7 standard deviations. The new magnetic moment, with a quantum electrodynamics (QED) calculation, determines the fine structure constant with a 0.7 ppb uncertainty [8, 9] – ten times smaller than for atom-recoil determinations. Remarkably, this 100 mK measurement probes for internal electron structure at 130 GeV.

A big additional reduction in the measurement accuracy is soon to be announced, based upon a new measurement for which the analysis is nearly finished.

2   Quantum Cyclotron

The quantum limit of an electron cyclotron accelerator was demonstrated and reported in collaboration with my student S. Peil [4].

When the cyclotron is cooled to 80 mK, 50 times lower than previously realized with an isolated elementary particle, quantum nondemolition (QND) measurements show that the electron stays in the ground state of its cyclotron motion for hours, leaving only in response to resonant photons deliberately introduced from outside. At higher temperatures, blackbody photons are present in sufficient numbers to occasionally excite the electron cyclotron motion. QND measurements show the cyclotron oscillator remains in an excited energy eigenstate for many seconds before making an abrupt quantum jump to an adjacent state. The striking isolation of the electron from its environment is due to a 140-fold cavity-induced suppression of the spontaneous emission of synchrotron radiation. Analysis of the quantum jumps provides a way to measure the temperature of the electron, the average number of blackbody photons, and the spontaneous emission rate. Quantum jump spectroscopy provides a way to precisely measure the frequency separation of the lowest quantum states. A variety of applications are mentioned in conclusion.

The quantum cyclotron provides an unusual opportunity to observe and manipulate long lived states of a harmonic oscillator. When written in terms of raising and lowering operators, the Hamiltonian of the two dimensional cyclotron $H_c = h\nu_c(a^\dagger a + 1/2)$ is formally equivalent to that of the familiar one dimensional harmonic oscillator. The energy eigenstates of the electron cyclotron ($|n = 0\rangle$, $|n = 1\rangle$, ... in Fig. 1a) are often called Landau levels. They are formally equivalent to the familiar number states of the harmonic oscillator, often called Fock states in quantum optics. Though these states are well known to every student of quantum mechanics, the production, observation and use of Fock states in experiments is surprisingly difficult and rare. The unusually high probability $P > 0.999$ to be in the ground state of the quantum cyclotron, and the extremely long lifetime of the Fock states, should make it possible to excite any superposition of the lowest Fock states with a properly tailored sequence of drive pulses.

We reported the nondestructive observation of Fock states as high as $|n = 4\rangle$. At the time of this observation, only zero- and one-photon Fock states, $|n = 0\rangle$ and $|n = 1\rangle$, had previously been observed for a radiation mode of a cavity [10, 11], though efforts were underway to observe two-photon and higher Fock states [12]. A ground state occupation fraction $P = 0.95$ was reported. Vibrational Fock states of a laser-cooled Be^+ ion in a potential well have also been selectively excited, starting from a similar ground state occupation of $P = 0.95$ [13]. The formation of these Fock states was deduced destructively, from repeated measurements which transferred the
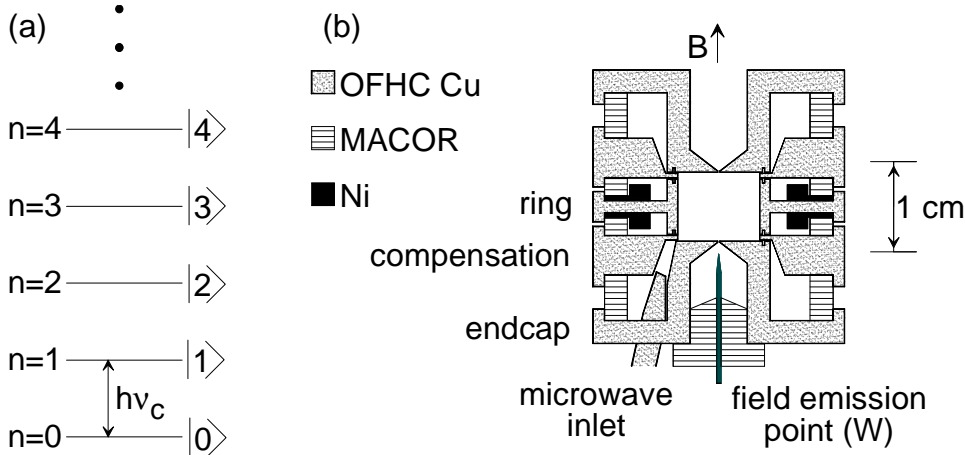
Figure 1: (a) Energy levels of the one-electron cyclotron oscillator. (b) Electrodes of the cylindrical Penning trap cavity.

population of identically prepared states to internal energy levels, whose monitored time evolution revealed the original state. Very recently, the $|n = 0\rangle$ and $|n = 1\rangle$ Fock states of neutral atoms oscillating in a one dimensional harmonic well were also observed [14] with $P = 0.92$ for the ground state. More recently, very nice observations of the Fock states of a radiation mode in a cavity show quantum jumps that look very much like those of our cyclotron oscillator [15, 16].

The quantum cyclotron is realized with a single electron stored in a cylindrical Penning trap [4, 2] that is cooled by a dilution refrigerator. The trap cavity (Fig. 1b) is a good approximation to a cylindrical microwave cavity at frequencies up to 160 GHz [17]. Tiny slits (125 μm) in the walls of the cavity make it possible to apply a trapping potential between the central ring electrode and the two flat endcap electrodes. The small slits include quarter wave "choke flanges" to minimize the loss of microwave radiation from the cavity. The potential is made a better approximation to a harmonic potential along the central symmetry axis of the trap by tuning an additional voltage applied to the two compensation electrodes.

Cavity radiation modes that couple to the cyclotron oscillator [17, 18] have quality factors as high as $Q = 5 \times 10^4$. The energy in a 150 GHz mode with this Q value damps exponentially with a 50 ns time constant that is very short compared to all relevant time scales. (The frequency widths of the cavity mode resonances, for example, are much wider than the oscillator's cyclotron resonance width.) The radiation modes of the cavity are thus thermal states with the temperature of the trap cavity. Thermal contact to a dilution refrigerator allows us to adjust the trap temperature between 4.2 K and 70 mK (only to 80 mK when our detector is on.) We detune the frequency of the one-electron cyclotron oscillator away from the radiation modes to decrease the spontaneous emission rate.

Two of the three motions of a trapped electron (charge $-e$ and mass m) in a Penning trap [19] are relevant to this work. Our central focus is upon the circular cyclotron motion, perpendicular to a vertical 5.3 T magnetic field, with cyclotron frequency $\nu_c = eB/(2\pi m) = 147$ GHz and energy levels separated by $h\nu_c$. The Fock states $|n\rangle$, often called Landau states for the particular case of a charged particle in a magnetic field, decay via spontaneous emission to $|n - 1\rangle$ at a rate

$n\gamma$, where γ is the classical decay rate of the oscillator. In free space for our field, $\gamma = (4\pi\epsilon_o)^{-1}16\pi^2\nu_c^2 e^2/(3mc^3) = (94 \text{ ms})^{-1}$. This is the rate that is inhibited by the trap cavity.

The electron is also free to oscillate harmonically along the direction of the vertical magnetic field, $\hat{z}$, at a frequency $\nu_z = 64$ MHz $\approx \nu_c/1000$. We drive this axial motion by applying an oscillatory potential between the ring and an endcap electrode, and detect the oscillatory current induced through a resonant tuned circuit attached between the ring and the other endcap. The electron axial motion damps as energy dissipates in the detection circuit, yielding an observed resonance width of 5 Hz for the driven axial motion. With appropriate amplification and narrow bandwidth detection we are able to measure small (1 Hz) shifts in ν_z. A heterostructure field effect transistor (HFET), constructed with Harvard collaborators just for these experiments, provides the radiofrequency gain that is needed while dissipating only 4.5 μW. The dilution refrigerator had difficulty with the nearly 700 times greater power dissipation (3 mW) of the conventional MESFET used initially.

The cyclotron and axial motions of the electron would be uncoupled except that we incorporate two small nickel rings into the ring electrode of the trap (Fig. 1b). These saturate in and distort the otherwise homogeneous magnetic field. The resulting "magnetic bottle",

$$\Delta\vec{B} = B_2 \left[\left(z^2 - (x^2 + y^2)/2\right) \hat{z} - z(x\hat{x} + y\hat{y}) \right], \qquad (1)$$

is similar to but much bigger than what was used to determine an electron spin state [20]. Coupling the combined cyclotron and spin magnetic moment $\vec{\mu}$ to $\Delta\vec{B}$ gives a term in the Hamiltonian that is harmonic in z,

$$V = -\vec{\mu} \cdot \Delta\vec{B} = 2\mu_B B_2(a^\dagger a + 1/2 + S_z/\hbar)z^2, \qquad (2)$$

where μ_B is the Bohr magneton, S_z is the spin operator, and the electron g value is taken to be 2. This V makes ν_z shift in proportion to the energy in the cyclotron and spin motions,

$$\Delta\nu_z = \delta(n + 1/2 + m_s). \qquad (3)$$

A one quantum excitation of the cyclotron oscillator shifts the monitored ν_z by $\delta = 2\mu_B B_2/(m\omega_z) = 12.4$ Hz, substantially more than the 5 Hz axial linewidth and the 1 Hz resolution.

The measurement of the cyclotron energy is an example of a QND measurement [21, 22] in that V and H_c commute, $[V, H_c] = 0$. The desirable consequence is that a second measurement of the cyclotron energy at a later time will give the same answer as the first (unless a change is caused by another source). This is not generally true for measurements with a quantum system. For example, measuring the position of a free particle would make its momentum completely uncertain. After additional time evolution a second measurement of the particle's position would give a different outcome.

Five one-hour sequences of QND measurements of the one-electron oscillator's energy are shown in Fig. 2. Each is for a different cavity temperature T, as measured with a ruthenium oxide sensor attached to the ring electrode. Greatly expanded views of several quantum jumps are shown in Fig. 3. Energy quantization is clearly visible, as are the abrupt quantum jumps between Fock states. The upward quantum jumps are absorptions stimulated by the blackbody photons in the trap cavity. The

downward transitions are spontaneous or stimulated emissions. Mostly we see the oscillator in its ground state $|n = 0\rangle$, with occasional quantum jumps to excited Fock states. Fig. 3b shows a rare event in which 4.2 K blackbody photons sequentially excite the one-electron cyclotron oscillator to the Fock state $|n = 4\rangle$. It takes of order 2 s of signal averaging for us to ascertain the quantum state of the cyclotron oscillator. This true measurement time is less, being the time required to establish the quantum state in principle. An estimate of this time [23] unfortunately uses assumptions that do not correspond well to the experimental conditions.

We analyze the quantum jumps to measure the temperature of the cyclotron oscillator, T_c. The measured probabilities P_n for occupying Fock states $|n\rangle$, averaged over many hours, are shown to the right in Fig. 2 for each cavity temperature. The measured P_n fit well to the Boltzmann factors $P_n = Ae^{-nh\nu_c/kT_c}$ which pertain for thermal equilibrium, demonstrating that averaged over hours the oscillator is in a thermal state. The fit determines T_c. Measurements with this "quantum Boltzmann thermometer" (solid points in Fig. 4a) shows that T_c is equal to the cavity temperature T; the cyclotron oscillator is in thermal equilibrium with the blackbody photons in the cavity. The solid points in Fig. 4b show the measured average quantum number superimposed upon the curve $\bar{n} = [e^{h\nu_c/kT} - 1]^{-1}$ which pertains for an oscillator in thermal equilibrium at the measured cavity temperature T. For temperatures of 4.2 K, 1 K and 80 mK, $\bar{n}$ varies dramatically from 0.23, to 9×10^{-4}, to 6×10^{-39}.
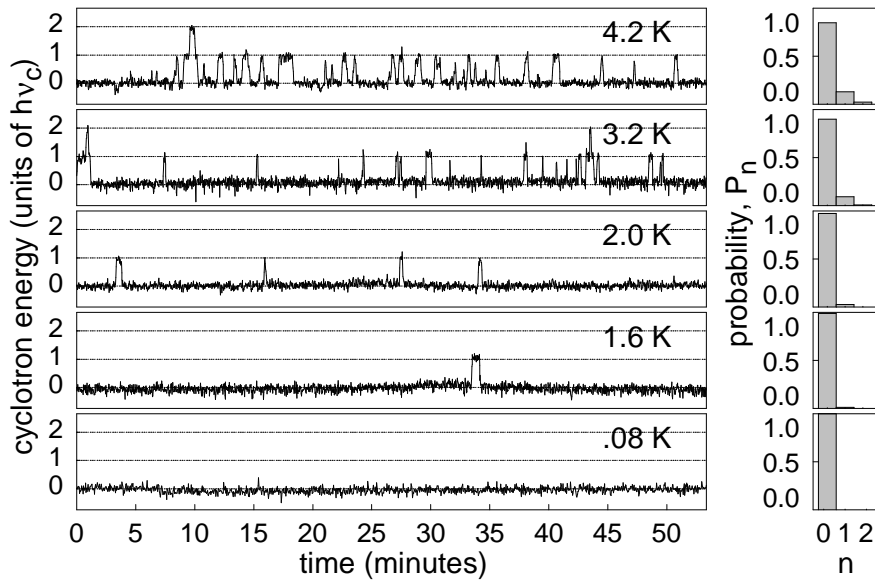

Figure 2: Quantum jumps between the lowest states of the one-electron cyclotron oscillator decrease in frequency as the cavity temperature is lowered.

Below 1 K the oscillator resides in its ground state for so long (we estimate 10^{32} years for 80 mK) that it is difficult to directly measure the oscillator temperature T_c. The best we can do is to establish that at some confidence level C, this temperature is below a limit given by $kT_c \le h\nu_c/\ln[1 - \gamma t/\ln(1 - C)]$ if we observe no excitation for time t. When no excitation is observed for $t = 5$ hours, for example, we establish that $T_c < 1.0$ K at the $C = 68\%$ confidence level. For temperatures below 1 K, blackbody photons have been essentially eliminated, and the one-electron cyclotron
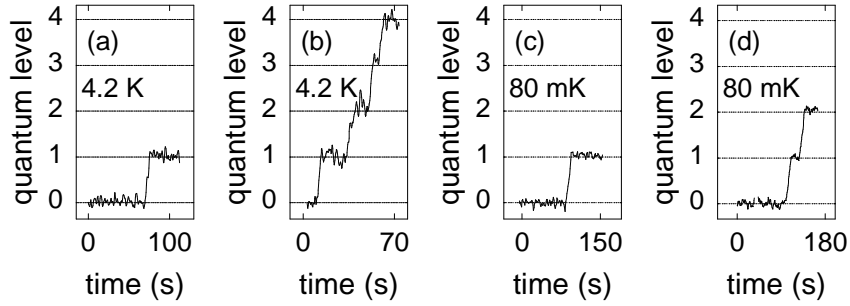
Figure 3: Excitations to excited Fock states which are stimulated by 4.2 K blackbody photons in (a) and (b), and by an externally applied microwave field in (c) and (d).

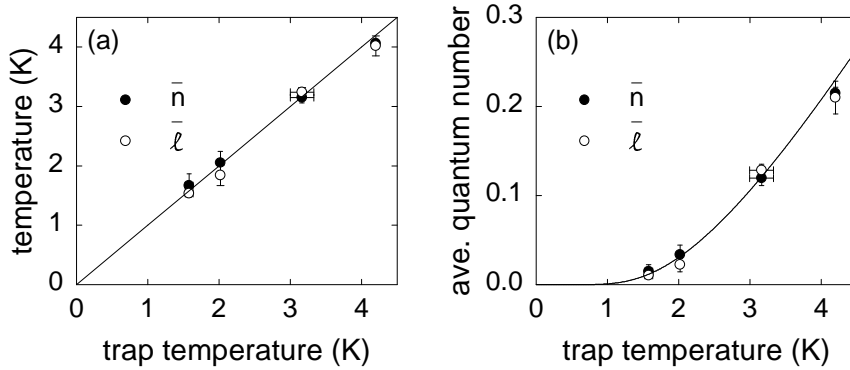oscillator is virtually isolated from its environment.

Figure 4: (a) The oscillator temperatures deduced from the measured occupation times in each number state (solid points) and deduced from the transition rates (open points) are compared to the temperature of a ruthenium oxide thermometer attached to a trap electrode. (b) Measured average values $\bar{n}$ and $\bar{\ell}$ as a function of cavity temperature.

We can separately measure the rate Γ_{abs} for the upward jumps (corresponding to stimulated absorption), and the rate Γ_{em} for downward jumps (corresponding to stimulated and spontaneous emission together). For $T = 1.6$ K, Fig. 5 shows a histogram of the dwell times in $|n = 0\rangle$ in (a) and for $|n = 1\rangle$ in (b). Both histograms decrease exponentially, indicating random processes, so the fitted lifetimes $(\Gamma_{abs})^{-1}$ and $(\Gamma_{em})^{-1}$ are just the average values of the dwell times. The rates for stimulated emission from $|n\rangle$ to $|n-1\rangle$ and for stimulated absorption from $|n-1\rangle$ to $|n\rangle$ are expected to be equal by the principle of detailed balance. Thus the spontaneous emission rate is simply the difference between the observed emission rate and the observed absorption rate, $\gamma = \Gamma_{em} - \Gamma_{abs}$. At $T = 1.6$ K (Fig. 5) the measured stimulated absorption rate is negligibly smaller so that $\gamma^{-1} \approx \Gamma_{em}^{-1} = 13$ s.

Comparing the 13 s spontaneous emission lifetime that is measured with the 94 ms expected for free space shows that spontaneous emission of synchrotron radiation is strongly suppressed. The 140-fold inhibition is due to the copper trap cavity that encloses the electron oscillator [24]. By adjusting the magnetic field, the frequency of the cyclotron oscillator is tuned away from resonance with the radiation
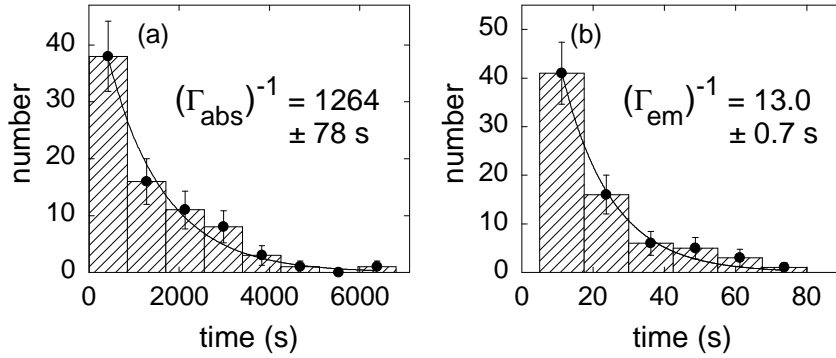
Figure 5: Histograms of the dwell times preceding stimulated absorption from $n = 0$ to $n = 1$ in (a), and for spontaneous and stimulated emissions from $n = 1$ to $n = 0$ in (b), both for $T = 1.6$ K. Dwell times less than 5 s are excluded since short dwell times are obscured by detection time constants.

modes of the trap cavity. The electron oscillator then couples only very weakly to the modes of the radiation field, and spontaneous emission is suppressed. We would not otherwise be able to signal average sufficiently to observe the quantum jumps so distinctly, nor would the excited Fock states persist so long.

The measured emission and absorption rates determine the average number $\bar{\ell}$ of resonant blackbody photons within the cavity. Quantum electrodynamics indicates that stimulated emission from $|n\rangle$, and stimulated absorption into $|n\rangle$, both have the same rate given by $\bar{\ell}n\gamma$. Applied to $n = 1$, this means that $\Gamma_{abs} = \bar{\ell}\gamma$ and $\Gamma_{em} = (1 + \bar{\ell})\gamma$. The average number of blackbody photons in terms of measurable quantities is thus given by $\bar{\ell} = \Gamma_{abs}/(\Gamma_{em} - \Gamma_{abs})$. The measured open points in Fig. 4b agree well with the expected curve $\bar{\ell} = [e^{h\nu_c/kT} - 1]^{-1}$, and $\bar{n} = \bar{\ell}$ as predicted. Fitting to the measured $\bar{\ell}$ gives an independent measurement of the temperature of the cavity (open points in Fig. 4a). These agree well with the directly measured cavity temperature.

Extremely precise quantum jump spectroscopy of the lowest levels of the quantum cyclotron should become possible with blackbody photons eliminated from the trap cavity. Quantum jumps (e.g. Fig. 3c-d) will take place only when externally generated microwave photons are introduced into the trap cavity, increasing in rate as the drive frequency is swept through resonance. One challenge is that the z^2 term in the magnetic bottle (Eq. 1) not only couples ν_z to the cyclotron energy (Eq. 3) as is desired for good detection sensitivity. It also shifts the cyclotron frequency in proportion to the axial energy E_z with $\Delta\nu_c = \delta E_z/(h\nu_z)$. The measured distribution of cyclotron frequencies shows that the current axial detector heats the axial motion of the electron to 17 K, well above the 80 mK temperature of the trap and cyclotron motion. However, the long lifetime of the first excited Fock state should make it possible to introduce microwave photons while the axial motion is cooled to 80 mK, before turning on the axial detector to observe whether a cyclotron excitation has been made.

In conclusion, a quantum cyclotron is demonstrated using one electron in a cylindrical Penning trap cavity. QND measurements of quantum jumps between cyclotron Fock states shows that the temperature of the cyclotron motion tracks the

cavity temperature where this can be measured, from 4.2 K to 1.6 K. At 80 mK the electron is 50 times colder than previously demonstrated for an isolated elementary particle. Blackbody photons are completely absent and the cyclotron remains in its quantum ground state. The jumps also show that the Fock states are long lived; the cavity suppresses the spontaneous emission of synchrotron radiation 140-fold.

The quantum cyclotron is so well prepared in its ground state, and so well isolated from its environment, that it may be possible to excite any desired superposition of excited states, to probe the nature of decoherence and quantum measurement. Quantum jump spectroscopy offers the prospect to measure the frequency between the lowest Fock states (and spin states) with the exquisite precision required to significantly improve the very accurate measurement of the the electron magnetic moment and the fine structure constants, as illustrated in following sections. A better lepton CPT test, comparing the magnetic moments of the electron and positron, should be possible, along with a better measurement of the proton-to-electron mass ratio.

The work of this section was done as part of the Ph.D. work of S. Peil, with early experimental contributions from K. Abdullah and D. Enzer. Support came from the NSF with some assistance from the ONR.

3   Feedback Cooling

Feedback cooling of the axial motion of a single suspended electron in a cylindrical Penning trap was initially reported in collaboration with my students B. D'Urso, and B. Odom [5].

At a time when the importance of feedback for reducing amplifier noise was already recognized [25], Kittel described the theory and limits of "noiseless" feedback damping [26]. Feedback damping has been applied in subsequent decades to a variety of oscillatory systems including an electrometer[27], a torsion balance [28], a mechanical gravity gradiometer [29], a laboratory rotor [30], a vibration mode of an optical mirror [31], and to the stochastic cooling of particle beams [32]. The possible application of Kittel's "noiseless" feedback to trapped particles was mentioned [33], as was the relevance of the limitations he discussed [34] to proposed stochastic cooling of trapped antiprotons [35]. Using feedback to improve measurements is an active area of current research [36].

This section describes the feedback cooling of the simplest of oscillators – one with demonstrated potential for fundamental measurements. A one-electron oscillator is cooled from 5.2 K to 0.85 K. A unique feature is that this classical oscillator's temperature and damping rate are both determined absolutely by measuring frequencies. A novel feature is that quantum jump thermometry (utilizing quantum electron cyclotron motion orthogonal to the cooled classical oscillation) directly displays the Boltzmann distribution of oscillator energies [4]. The measurements reveal cooling to an ideal, noiseless feedback limit that is characterized by a fluctuation-dissipation invariant. Noise added by the active feedback electronics limits the lowest temperature attained.

The observed narrowing of an electron's cyclotron resonance line, with similar narrowing of the "anomaly" resonance [19] at the difference of its spin and cyclotron frequencies, will allow higher precision measurements of these frequencies and more precise systematic studies. The higher accuracy determination of these frequencies

expected as a result could enable better measurements of the magnetic moments of the electron and positron, an improved determination of the fine structure constant, an improved CPT test with leptons, and a better measurement of the proton-to-electron mass ratio.

The oscillation cooled with feedback is that of a single electron along the central symmetry axis ($\hat{z}$) of a cylindrical Penning trap [1, 2] (Fig. 6). The trap electrodes are biased so the electron oscillates in a harmonic potential well ($\sim z^2$) with frequency $\nu_z = 64.787$ MHz. The z^4 well distortion is tuned out by adjusting the potential on small, orthogonalized compensation electrodes [1].
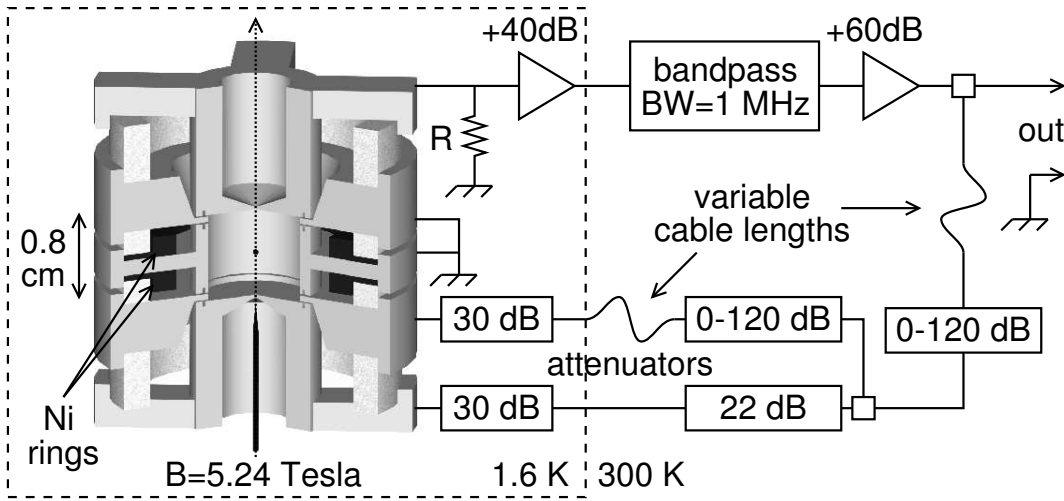

Figure 6: Representation of trap and high frequency electronics used for feedback cooling. Static potentials applied to suspend the electron at the trap center are not shown.

We treat the one-electron oscillator as a charge attached to a massless spring, focussing upon potentials and currents that oscillate near ν_z, while ignoring the additional static trapping potentials always applied to the trap. Oscillatory potentials applied to either of the two endplate electrodes (Fig. 7) drive the electron oscillator. The electron motion, in turn, induces a current I to flow through R, a resistance due to unavoidable loss in an attached amplifier and inductor. The inductor (in parallel to R but not shown) tunes out trap capacitance (e.g. between the plates).

With no feedback (Fig. 7a), the induced current I removes energy from the electron oscillator at the familiar rate I^2R, with the result that the damping rate $\Gamma \propto R$. The proportionality constant depends upon the electron charge, the electron mass and the geometry of the trap [19]. Measurements to be discussed show that the electron oscillator is weakly damped (i.e. $\Gamma/2\pi \ll \nu_z$) with $\Gamma/2\pi = 8.4$ Hz.

The random thermal fluctuations of electrons within R, in thermal equilibrium at temperature T, produce a fluctuating Johnson-Nyquist noise potential [37, 38] V_n. This frequency independent white noise, with

$$\overline{V_n^2} = 4kTR\Delta\nu \tag{4}$$

in a frequency bandwidth $\Delta\nu$, drives the electron. This noise and the induced current both contribute to the voltage on the upper plate, $V = V_n + IR$. A sensitive HEMT (high electron mobility transistor) amplifier amplifies V so it can be detected.
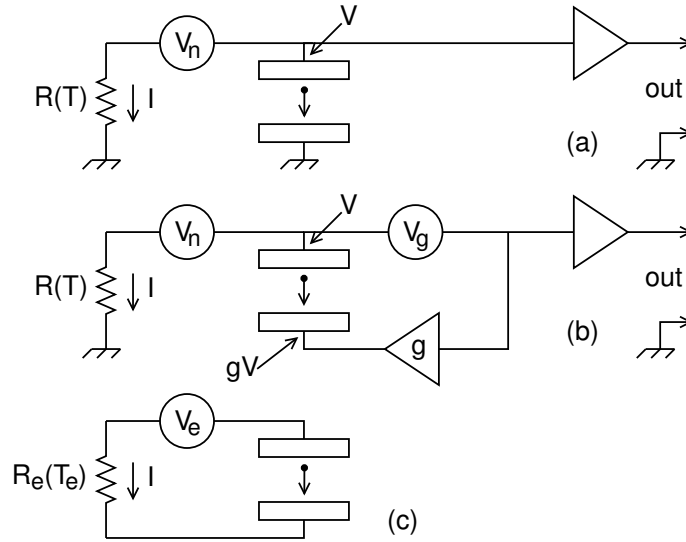
Figure 7: Conceptual circuit without (a) and with (b) feedback. For ideal noiseless feedback, $V_g = 0$. For the electron, circuits (b) and (c) are equivalent.

The measured power spectrum for V (Fig. 8a) has a constant baseline due to the Johnson noise. The current induced by the noise-driven electron produces a notch in this flat spectrum at ν_z; the angular frequency width of this notch is the damping rate Γ. The notch is most easily understood if the oscillating charge is represented as a familiar electrical oscillator, an inductor ℓ and a capacitor c in series, connected between the plates. On resonance at ν_z the electron acts as an electrical short between the plates since the reactances of the ℓ and c cancel. The notch has the characteristic Lorentzian shape of a damped harmonic oscillator. The observed noise cancellation is not perfect (i.e. the dip does not go perfectly to zero power in Fig. 8a) because of amplifier noise, trap potentials that are not perfectly stable, and residual trap anharmonicity.
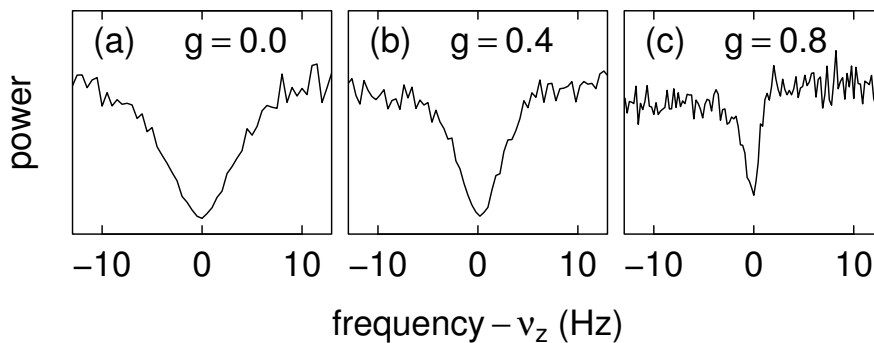

Figure 8: Oscillator damping rate Γ_e (the width of the notch in the white Johnson noise) without feedback (a) and when decreased using feedback (b)-(c).

When the amplifier is on, as it must be for feedback to be applied, measurements to be discussed show that R is at a temperature of 5.2 K. This is higher than the 1.6 K of the trap apparatus (maintained by thermal contact to a pumped ^{4}He system), despite the minimal 420 μW power dissipation of the current-starved HEMT, and

heroic efforts to thermally anchor the HEMT at 1.6 K.

Feedback is applied as shown conceptually in Fig. 7b. The fluctuating upper plate voltage V is fed back to the lower plate with feedback gain, g. A more complete representation (Fig. 6) shows amplifiers, attenuators and variable cable lengths used to adjust the feedback phases. Correctly phased feedback to two electrodes, rather than just to the bottom plate in the conceptual Fig. 7b, applies feedback to the electron while canceling feedback to the amplifier. Feedback to the amplifier would modify its properties [25], perhaps improving particle detection in some situations [39], but would complicate the relationship between feedback gain, electron temperature and electron damping.

For the electron, the effect of feedback is equivalent to the circuit in Fig. 7c, with R_e and T_e chosen to make the motion-induced potential and the fluctuation potential across the plates the same as for Fig. 7b.

To determine R_e (and hence the damping rate $\Gamma_e \propto R_e$) we insist that electron motion induces the same potential difference across the plates. Equating $IR - gIR$ for Fig. 7b with IR_e for Fig. 7c yields $R_e = (1 - g)R$, and an electron damping rate

$$\Gamma_e = (1 - g)\Gamma. \tag{5}$$

When $g = 0$ we recover the damping rate Γ for no feedback. When $g = 1$ the electron oscillator is undamped.

To determine the effective temperature T_e we insist that the electron see the same noise fluctuations across the plates in Figs. 7b and 7c. Equating $V_n - gV_n$ for Fig. 7b with V_e for Fig. 7c, yields

$$T_e = (1 - g)T. \tag{6}$$

We recover the resistor temperature T when there is no feedback ($g = 0$). The temperature decreases as the feedback gain is increased. We shall see that noise added in the feedback process prevents attaining 0 K as $g \to 1$.

The fluctuations (characterized by a temperature) and the dissipation (characterized by a damping rate) are related for ideal, noiseless feedback by a fluctuation-dissipation invariant [26],

$$T_e/\Gamma_e = T/\Gamma. \tag{7}$$

Noiseless feedback with gain $g < 0$ increases the damping rate but at the expense of also increasing the temperature and fluctuations. Noiseless feedback cooling, with $0 < g < 1$, decreases the temperature, but at the expense of reducing the damping rate. The advantage of a reduced T_e is to reduce deleterious effects of axial fluctuations upon other electron motions, as we will illustrate with a reduced cyclotron linewidth.

Real feedback amplifiers add fluctuations V_g that increase T_e above the the ideal Eqs. 6-7, and reduce the depth of the observed Lorentzian noise notch. Equating the fluctuations across the plates for Figs. 7b-c yields

$$T_e = T \left[1 - g + \frac{g^2}{1 - g} \frac{T_g}{T} \right]. \tag{8}$$

T_g is a feedback "noise temperature" such that $\overline{V_g^2}/\overline{V_n^2} = T_g/T$. The relative depth of the Lorentzian notch in the observed noise power,

$$F = 1 - (1 - g)^{-2}(1 + T/T_g)^{-1}, \tag{9}$$

is the ratio of this noise power on and off resonance.

T_e initially drops linearly with g increasing from zero as in the ideal case (Eq. 6). (An example is the function fit to measured temperatures in Fig. 10a, discussed later.) T_e then rises rapidly as $g \to 1$, the limit of an undamped oscillator driven by feedback noise.

The lowest temperature is $T_e(min) \approx 2\sqrt{T_g T}$, for $T_g \ll T$, is at an optimal feedback gain $g \approx 1 - \sqrt{(T_g/T)}$, and our amplifier has $T_g \approx 40$ mK. Meanwhile, the deep notch ($F \approx 1$ for $g = 0$) goes to essentially no notch at all ($F \approx 0$) at the gain that minimizes T_e. Damping remains but we cannot measure its rate by this method.

The temperature T_e of the effective damping resistance is important because the electron axial oscillation comes into thermal equilibrium at T_e. Averaged over many axial damping times Γ^{-1}, the probability that the oscillator has energy between E_z and $E_z + dE_z$ goes as the Boltzmann factor, e^{-E_z/kT_e}.

Remarkably, we can directly measure this Boltzmann distribution, and hence T_e, using quantum jump thermometry. The quantum jumps [4] are between the ground and first excited states of the electron's cyclotron motion in a 5.24 Tesla magnetic field directed along the electron's axial oscillation (Fig. 6). Compared to the rapid 146.7 GHz cyclotron motion the axial motion is adiabatic. It is unaffected by a single quantum cyclotron excitation except for the tiny shift of ν_z (Eq. 11) that we discuss next. The cyclotron damping lifetime is extended to 15 seconds (from 0.1 seconds for free space) using a trap cavity that inhibits spontaneous emission [4].

The coupling of cyclotron and axial motion comes from the small "magnetic bottle" gradient [19] from two small nickel rings (Fig. 6). The electron sees a magnetic field that increases slightly as z^2 as it moves away from the center of the trap in its axial oscillation. This coupling shifts the cyclotron frequency by a measured [4] $\delta = 12$ Hz for every quantum of axial excitation,

$$\Delta\nu_c = \delta(E_z/h\nu_z). \tag{10}$$

The axial frequency shifts by the same amount,

$$\Delta\nu_z = \delta(E_c/h\nu_c), \tag{11}$$

for every quantum of cyclotron excitation. Both tiny shifts are used for the quantum jump thermometry.

A Boltzmann distribution of axial energies, owing to Eq. 10, makes an associated distribution of cyclotron frequencies, given that the axial damping time is longer than the time associated with the noise fluctuations of the axial frequency [19]. A cyclotron driving force at frequency ν excites a quantum jump between the ground and first excited cyclotron states with a probability

$$P(\nu) \sim \begin{cases} 0, & \nu < \nu_c \\ e^{-\frac{\nu_z}{\delta}\frac{h(\nu-\nu_c)}{kT_e}}, & \nu > \nu_c, \end{cases} \tag{12}$$

provided that the jumps happen more rapidly than the one per hour stimulated by blackbody photons in the 1.6 K trap cavity.

To determine whether a quantum jump has taken place we look for the corresponding axial frequency shift (Eq. 11). We do not simply observe the center frequency of a noise dip (Fig. 8), though this would likely suffice. Instead, before

a cyclotron excitation decays (in typically 15 s), we observe the electron's response to a strong axial drive for the 1 second needed to measure $\Delta\nu_z$ and determine the cyclotron state.

The measurement cycle starts with 0.5 s of magnetron sideband cooling [19] to keep the electron near the center axis of the trap. Feedback cooling is then applied for 6 seconds, with the cyclotron drive at ν turned on for the last 2 of these seconds. The axial drive to determine $\Delta\nu_z$ and the cyclotron state is applied next, along with more magnetron cooling. The cyclotron state is read out once each second until the ground state is observed for 2 s. The cycle then repeats.
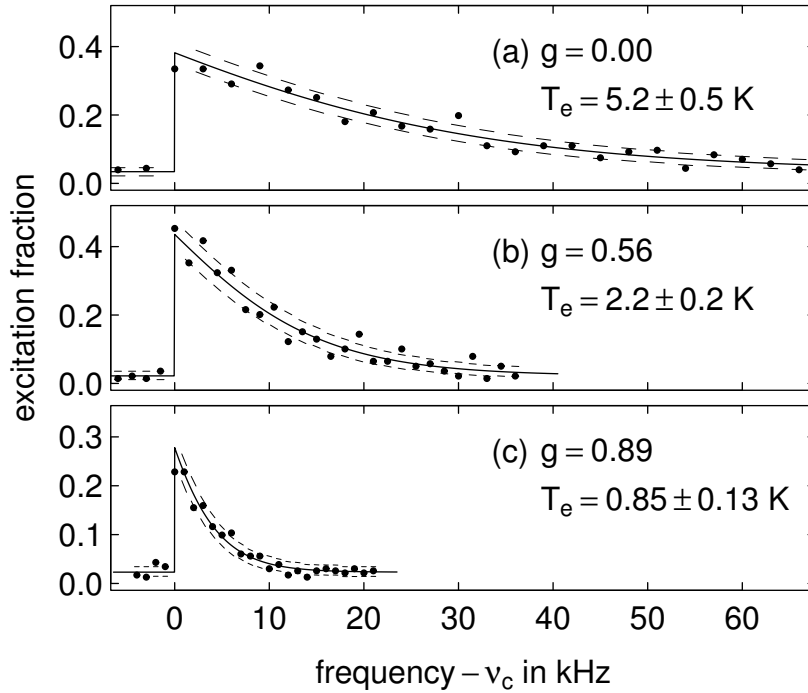

Figure 9: Cyclotron resonances show a Boltzmann distribution of axial energies that decreases as feedback gain g in increased. Dashed lines bound the 68% confidence area.

The measured cyclotron lineshapes (Fig. 9) narrow significantly as the feedback gain increases. Each shows the characteristic Boltzmann distribution that signifies thermal equilibrium. Each is fit to Eq. 12 to determine the equilibrium axial temperature, T_e. The lowest observed $T_e = 850$ mK (Fig. 9c) is a substantial reduction of the 5.2 K realized without feedback.

The measured axial temperature (Fig. 10a) decreases linearly as g increases from 0, as predicted in Eqs. 6 and 8. There is a good fit to Eq. 8, including the rapid increase for $g \to 1$ which corresponds to a nearly undamped system being driven by the noise added in the feedback signal. It is difficult to fix g accurately enough to measure points on this rapid rise.

The damping rate Γ_e, the width of a noise dip (e.g. Fig. 8), is measured directly (Fig. 10b). The damping rate decreases linearly with increasing g as predicted in Eq. 5. The vanishing dip width and the instabilities mentioned earlier keep us from measuring Γ near to $g = 1$.

Because we directly measure T_e (characterizing fluctuations) and Γ_e (character-
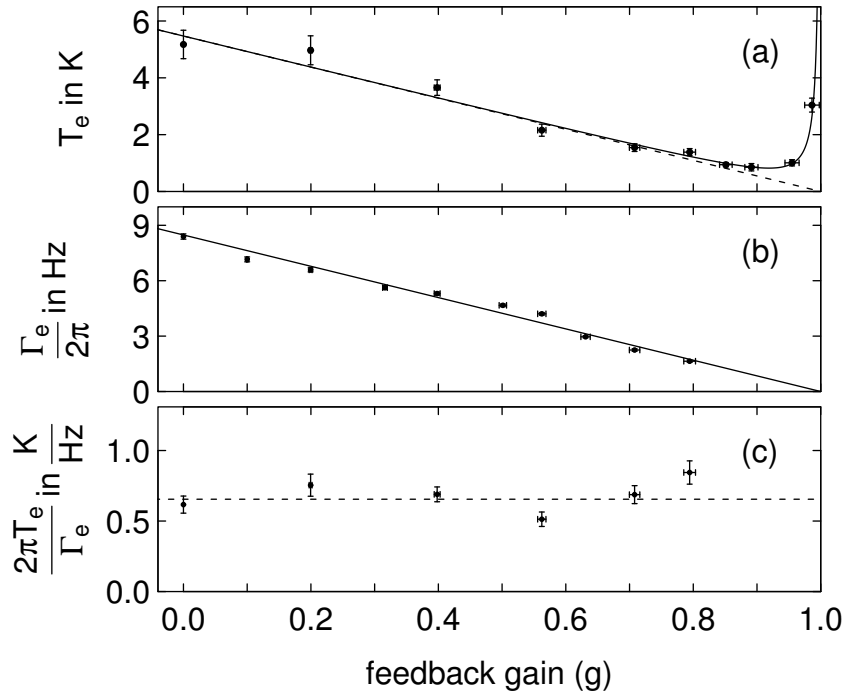
Figure 10: Axial temperature (a), damping rate (b) and the fluctuation-dissipation invariant (c) as a function of feedback gain. The dotted line in (c) is the weighted average.

izing dissipation) we can compare their ratio (Fig. 10c) to the fluctuation-dissipation invariant that pertains for noiseless feedback (Eq. 7). The measured ratio is invariant and is at the ideal limit, though we expect that it would rise above the ideal limit if we could measure it for feedback gains closer to unity.

In conclusion, feedback cooling to the noiseless limit is demonstrated with the simplest of oscillators. Characterization of the cooling of a one-electron oscillator is direct and complete because both fluctuations and dissipation are directly and absolutely determined by frequency measurements. In addition, sharply narrowed cyclotron lineshapes present the possibility of much more accurate measurements of the electron cyclotron frequency, with similar line narrowing and accuracy improvement expected for the electron "anomaly" resonance [19]. Better measurements of these frequencies for a single trapped electron and positron opens the way to better measurements of their magnetic moments, a more accurate value of the fine structure constant, a more precise test of CPT invariance for leptons, and an improved proton-to-electron mass ratio.

4   First One-Particle Self-Excited Oscillator

The initial demonstration of the use of electronic feedback to produce a one-particle self-excited oscillator was done in collaboration with my students B. D'Urso, R. Van Handel, B. Odom and D. Hanneke [6].
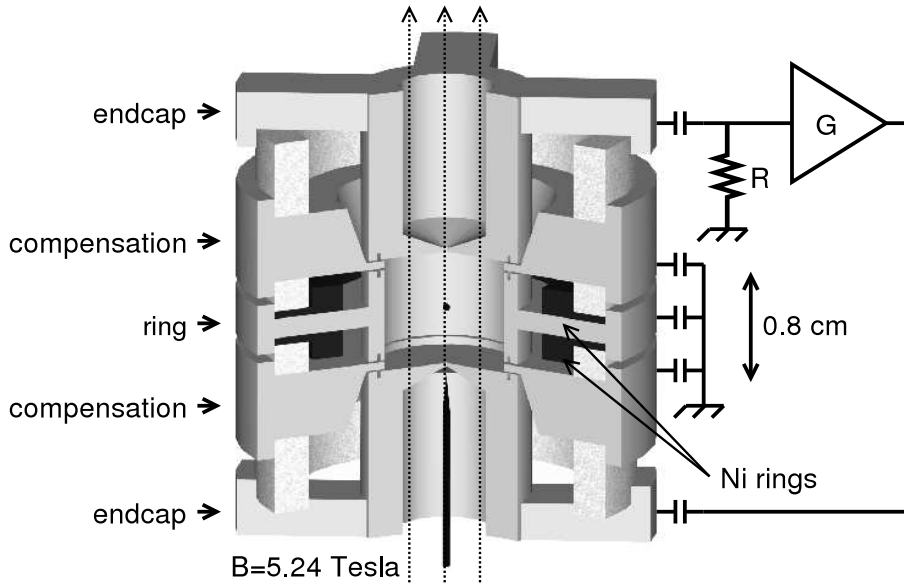
Figure 11: The vertical oscillation of a trapped electron, shown within a cutaway of a cylindrical Penning trap, induces a voltage across resistor R that is amplified and fed back to drive the oscillation. Unavoidable trap capacitance in parallel to R is tuned out at ω_z with a parallel inductor.

The harmonic motion of an oscillator can be excited and sustained with a driving force derived from its own oscillation. A wide range of macroscopic oscillators are operated as self-excited oscillators (SEO), from the electromechanical clock [40] and its ubiquitous quartz successors, to the nanomechanical cantilevers used in atomic force microscopes [41] and sensitive electrometers [42]. A microscopic SEO is more difficult to realize because such small signals and driving forces are involved. The possibility of realizing a one-ion SEO in a Paul trap was once discussed [33], and self-driven feedback cooling of a one-electron oscillator has been realized [5].

In this section we demonstrate a microscopic, one-particle SEO for the first time. The axial motion of a single electron suspended in a Penning trap is driven by an electric field derived from the current that its motion induces in an electrical circuit. The principal challenge is in stabilizing the electron's oscillation amplitude, an amplitude measured here using quantum jump spectroscopy of a perpendicular cyclotron motion. The frequency stability and the signal-to-noise allow detection of a 5 parts in 10^{10} frequency shift in a few seconds – a sensitivity that allows the detection of a one quantum change in the electron cyclotron energy and an electron spin flip. Likely applications are improved measurements of the electron, positron, proton and antiproton magnetic moments.

The oscillation which is self-excited is that of a single electron (charge $-e$ and mass m) along the central axis ($\hat{\mathbf{z}}$) of a cylindrical Penning trap [1] (Fig. 11) maintained at either 0.1 or 1.6 K. A ring electrode at potential $-V_0$ with respect to grounded endcaps generates a potential on the z-axis,

$$\Phi(z) = \frac{V_0}{2}\left[C_2\frac{z^2}{d^2} + C_4\frac{z^4}{d^4} + C_6\frac{z^6}{d^6} + \cdots\right], \tag{13}$$

where $d = 0.35$ cm indicates the trap size. The C_k are determined by trap geometry and by the potential V_c applied to small compensation electrodes (Fig. 11) to adjust

C_4 and C_6. An "orthogonalized" trap geometry [1] makes C_2 essentially independent of V_c.

A drive force $F_d(t)$ and a damping force $-m\gamma_z \dot{z}$ yield

$$\ddot{z} + \gamma_z \dot{z} + [\omega_z(A)]^2 z = F_d(t)/m. \tag{14}$$

The angular oscillation frequency $\omega_z(A)$ is

$$\frac{\omega_z(A)}{\omega_z} \approx 1 + \frac{3C_4}{4C_2}\left(\frac{A}{d}\right)^2 + \frac{15C_6}{16C_2}\left(\frac{A}{d}\right)^4, \tag{15}$$

for small $(C_4/C_2)^2$. It depends weakly upon the oscillation amplitude A [19], and $\omega_z = \sqrt{eV_0 C_2/(md^2)}$ pertains for small amplitudes.

The motion induces a voltage proportional to $\dot{z}$ across a $Q \approx 600$ tuned circuit (R in Fig. 11). Energy dissipated in R damps the motion. The signal is amplified with a high electron mobility transistor (Fujitsu FHX13LG) anchored to the cryogenic environment, and operated at a very low current to minimize trap heating. For the two realizations of the SEO that we will describe, typically 420 μW is used to detect the comparator SEO operated at 1.6 K, and only 12 μW for the DSP SEO at 0.1 K. Some amplified signal is phase shifted and fed back to the opposite endcap to drive the SEO. The rest is fourier transformed to determine its amplitude and the SEO oscillation frequency.

The feedback produces a force $F_d(t) = Gm\gamma_z \dot{z}$. Feedback cooling of the electron motion takes place if $G < 1$ [5]. Self-excitation occurs in principle when the feedback cancels the damping, for unit feedback gain $G = 1$. Any noise will cause amplitude diffusion and energy growth, however. Also, if G differs even slightly from unity, A will either decrease or increase exponentially.

A stable and useful SEO thus requires a fixed oscillation amplitude A_o, arranged using an amplitude-dependent gain $G(A)$ that decreases with increasing A near $G(A_o) = 1$. This gain in Eq. (14) yields

$$\dot{A} = -\tfrac{1}{2}\gamma_z A\left[1 - G(A)\right] \tag{16}$$

for the time evolution of the amplitude [43]. In practice, the gain-control system may average the signal for a time τ before determining A. Eq. (16) is valid if $\tau \gg 1/\omega_z$ and $1/\tau$ is much larger than the resulting self-excited oscillator linewidth.

We demonstrate two methods of stabilizing the amplitude of a SEO – passing the feedback drive through a comparator (Fig. 12a) and employing a fast digital signal processor or DSP (Fig. 12b). The first was realized at $\omega_z/(2\pi) = 64$ MHz and the second at $\omega_z/(2\pi) = 200$ MHz for reasons not related to this demonstration. The comparator is simpler, but the DSP is the more flexible option that can be made much more immune to noise. For both demonstrations the technical noise added by the feedback amplifier is so small [5] that we neglect it in our analysis. We were unable with the electrodes of our trap to realize a third method – applying the signal induced on one electrode to a second electrode (not the image of the first under $z \rightarrow -z$) to make the effective feedback gain decrease with oscillation amplitude.

A noiseless feedback drive passing through a comparator generates a fixed oscillation amplitude A_o. Thus $G(A) = A_o/A$ and Eq. (16) together yield

$$\dot{A} = -\tfrac{1}{2}\gamma_z(A - A_o). \tag{17}$$

(a)

```
                    ┌──────────┐
                    │    LO    │
                    │ v_z- 5 =MHz│
                    └────┬─────┘
signal                   │                 ┌──────┐        ┌──────────┐
in                       │           ┌─────┤  ∅   │────────│ variable │──────▶
  ┌──────────┐           │           │     └──────┘        │  atten.  │   drives
  │ bandpass │       ┌───▼──┐    ┌──────────┐   ┌──┐  ┌──────────┐ ┌──────────┐ out
──│ BW=5 MHz │───────│  ⊗   │────│ bandpass │───│⌐_│──│ bandpass │─│ variable │──▶
  └──────────┘       └──────┘    │ BW=150 Hz│   └──┘  │ BW=7.5 kHz│ │  atten.  │
                                 └──────────┘        └──────────┘ └──────────┘
```

(b)

```
              ┌──────────┐          ┌──────────┐
              │    LO    │          │    LO    │
              │ v_z - 5 MHz│        │ 4.995 MHz│
              └────┬─────┘          └────┬─────┘
                   │                     │
                   │  ┌──────────┐       │   ┌──────────┐  ┌──────────────┐
signal         ┌───▼──┐│ bandpass │  ┌───▼──┐│ bandpass │  │     DSP      │
in             │  ⊗   ││ BW=7.5 kHz│ │  ⊗   ││  BW=1 kHz │  │ TMS320F2812 │
  ┌──────────┐ └──────┘└──────────┘ └──────┘ └──────────┘  └──────────────┘ drive
──│ bandpass │──┘                                                            out
  │ BW=2 MHz │──────────────┌──────┐─────────────────────┌──────────────┐──▶
  └──────────┘              │  ∅   │                      │   voltage    │
                            └──────┘                      │variable atten.│
                                                          └──────────────┘
```
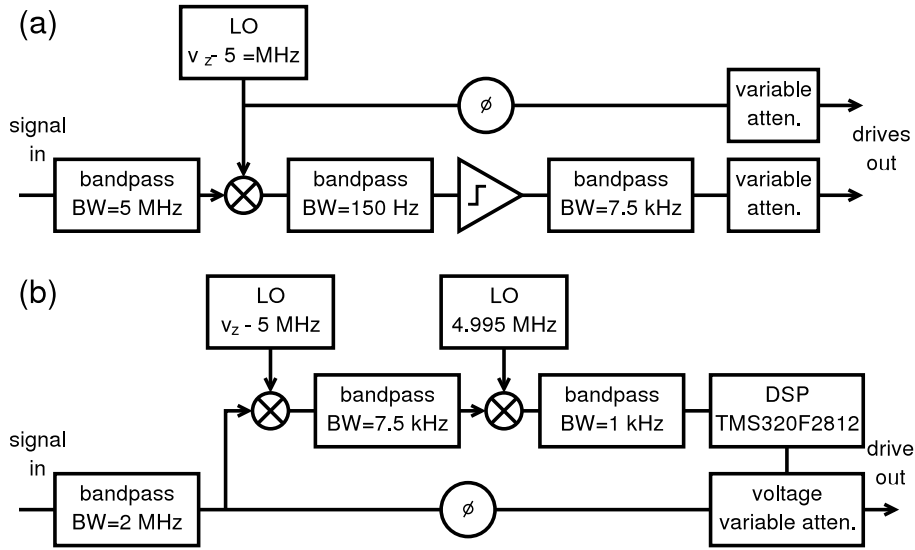
Figure 12: Overview of the comparator (a) and DSP (b) feedback used to obtain amplitude stabilization. Phase shifters are labeled with ϕ.

The amplitude A damps exponentially to A_o; the time constant $\gamma_z/2$ is the same as for damping without feedback. Noise injected into a comparator softens its gain response, limiting the gain at low A [44]. Narrow band filters (Fig. 12a) to reduce the noise are thus essential. A big challenge is in adjusting the trapping potential to keep the shifting oscillation frequency centered on the filters. (The drives to two electrodes in Fig. 12a are effectively one drive insofar as the electron mixes the two frequencies [19].)

We program the DSP chip to calculate a running Fourier transform of the amplified induced signal, and to adjust the feedback gain as a cubic function of the largest transform amplitude, so

$$\dot{A} = -\tfrac{1}{2}\gamma_z[a_1(A - A_o) + a_2(A - A_o)^2 + a_3(A - A_o)^3]. \tag{18}$$

For this demonstration only the linear term is used, with $a_2 = a_3 = 0$. The effective bandwidth (related to the fourier transform bin width) is 8 Hz, but the "filter" is always centered on the oscillation frequency. No square wave is generated so no filtering of harmonics is required.

Fig. 13 shows that $\omega_z(A_o) - \omega_z$ depends approximately quadratically upon A_o^2 as predicted by Eq. 15 for $A \ll d$. A_o is varied by changing the gain for three different V_c. A_o is determined from the size of the induced signal to which it is proportional, with a proportionality constant that will be discussed shortly. Fits of Eq. 15 to the measurements in Fig. 13 allow us to determine and adjust C_4 and C_6 with unprecedented accuracy.

One consequence is that extremely small frequency shifts can be quickly detected with the SEO. In a given averaging time, a frequency can typically be measured to the familiar limit provided by the uncertainty principle, divided by the signal-to-noise ratio (S/N) [45]. A large induced S is possible due to the large oscillation amplitudes, illustrated in Fig. 13. The effect of amplitude fluctuation noise N (driven by thermal fluctuations in the detection resistor) is particularly small if the oscillator amplitude is stabilized at a maxima (e.g. Fig. 13) caused when the
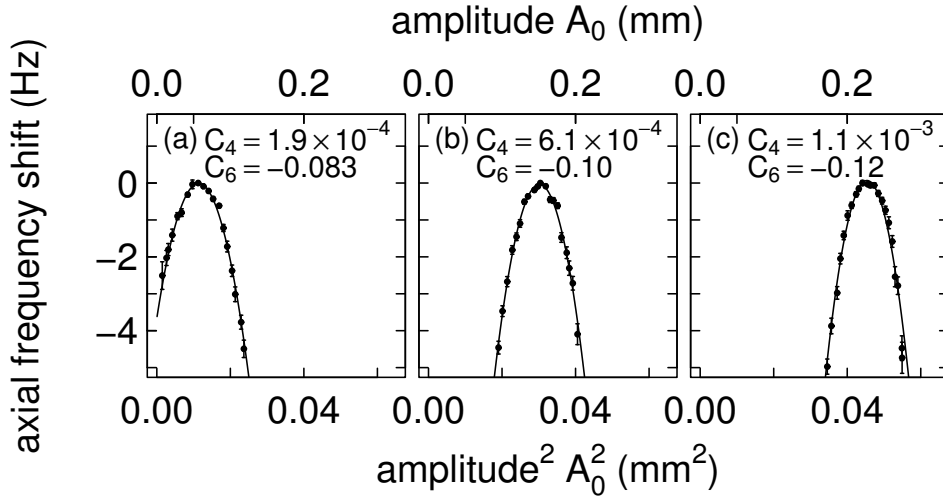
Figure 13: The axial frequency measured as a function of the square of the axial amplitude A_o using the comparator SEO.

effects of C_4 and C_6 of opposite sign cancel. An oscillator is locally harmonic at such maxima, with the oscillation frequency insensitive to small, noise-driven, amplitude fluctuations, despite the large oscillation in an anharmonic potential. Fig. 14a shows the standard deviation of repeated frequency measurements as a function of averaging time. With only four seconds of averaging time a 5 parts in 10^{10} (0.5 ppb) shift in ω_z can be measured – a substantial improvement on any other method.

In principle, a fixed frequency drive could sustain a large oscillation in an anharmonic potential. In practice, however, if the oscillator frequency changes suddenly the oscillation could be lost. Also, a fixed frequency drive cannot generally build up a large oscillation amplitude in the first place since the oscillator shifts out of resonance with the drive as the oscillation amplitude increases.

The considerable advantage of a SEO is that its self-derived drive always stays resonant, even if its oscillation frequency changes suddenly. It also stays resonant while the oscillation amplitude builds up to a large value, during which time the oscillation frequency is shifting. Typically our SEO is excited in less than 1 second.

A calibration of the axial oscillation amplitude – using quantum jump spectroscopy of an orthogonal cyclotron motion – is next. Noise applied to the oscillator gives a distribution of axial energies E_z about the stable oscillation energy E_o, amplitude A_o and phase ϕ_o that pertain for no noise. A reservoir at temperature T_z, weakly coupled to the axial motion, gives a distribution [46]

$$P(E_z; E_o, T_z) = \frac{1}{kT_z} e^{-\frac{E_z + E_o}{kT_z}} I_0 \left(\frac{2\sqrt{E_z E_o}}{kT_z} \right), \tag{19}$$

where I_0 is a modified Bessel function. No feedback drive gives $E_o \to 0$ and a Boltzmann distribution of E_z.

A simple derivation verifies this distribution and highlights the assumptions. For small fluctuations from A_o the oscillation can be taken as harmonic at angular frequency $\omega_o = \omega_z(A_o)$, with $E_o = \frac{1}{2}m\omega_o^2 |A_o e^{i\phi_o}|^2$. Noise alone would drive the oscillator into thermal equilibrium, to a Boltzmann distribution of energies $E_n = \frac{1}{2}m\omega_o^2 |A_n e^{i\phi_n}|^2$, where ϕ_n is a random oscillation phase. The oscillation amplitude
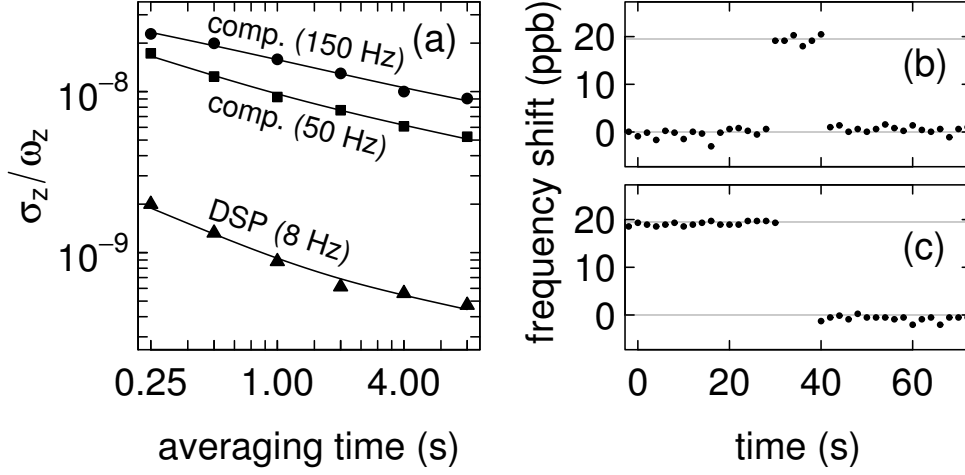
Figure 14: Fractional standard deviation of repeated frequency measurements for SEO with indicated bandwidth (a). Small shifts in the frequency of a 200 MHz SEO indicate a one-quantum cyclotron excitation (b) and a separate spin flip (c). The SEO is off while a drive is applied to flip the spin, giving the gap in (c).

A_z and phase ϕ_z due to independent feedback and noise drives is the superposition $A_z e^{i\phi_z} = A_o e^{i\phi_o} + A_n e^{i\phi_n}$ for a harmonic oscillation. The combined effect of feedback and noise for a particular ϕ_n arises from the distribution of the total amplitude

$$\tilde{P}(A_z e^{i\phi_z}) \propto e^{-\frac{E_n}{kT_z}} = e^{-\frac{m\omega_o^2 |A_z e^{i\phi_z} - A_o e^{i\phi_o}|^2}{2kT_z}}. \tag{20}$$

The probability distribution of $E_z = \frac{1}{2}m\omega_o^2 |A_z e^{i\phi_z}|^2$ in Eq. 19 is the average of this distribution over random ϕ_z.

Remarkably, quantum jump spectroscopy directly measures Eq. 19 and thus determines A_o and T_z. The quantum jumps [4] are between the ground and first excited states of cyclotron motion at frequency $\nu_c = 148$ GHz in a $B = 5.24$ Tesla magnetic field $B\hat{\mathbf{z}}$. A small "magnetic bottle" gradient $\Delta\mathbf{B} \sim z^2\hat{\mathbf{z}}$ [47] from two nickel rings (Fig. 11) weakly couples the cyclotron (or spin) magnetic moment μ to the axial motion, adding a coupling term that goes as $\mu\Delta B \sim \mu z^2$ to the Hamiltonian.

The corresponding small addition to the oscillator's restoring force, $\sim \mu z$, shifts the observed axial oscillation frequency in proportion to μ. Our frequency resolution makes it possible to observe that ω_z shifts by δ for a single quantum excitation from the cyclotron ground state (Fig. 14b). The probability P_c that a cyclotron driving force at a frequency ν causes a quantum jump [4] thus becomes measurable. For the 200 MHz oscillator, $\delta = 3.9$ Hz. For the 64 MHz oscillator, $\delta = 12$ Hz.

The second consequence of the magnetic bottle coupling is that the magnetic field averaged over an axial oscillation changes with oscillation energy, shifting ν_c by δ for every quantum of axial energy. The quantum jump spectrum,

$$P_c(\nu; E_o, T_z) \propto P(\hbar\omega_z(\nu - \nu_c)/\delta; E_o, T_z), \tag{21}$$

thus reveals the distribution of axial energies of Eq. 19.

Figs. 15a-c show examples for the three axial oscillation amplitudes that result for the trap settings of Fig. 13a-c. The extracted temperature T_z (Fig. 15d) is independent of oscillation amplitude. The detection amplifier makes T_z hotter than the
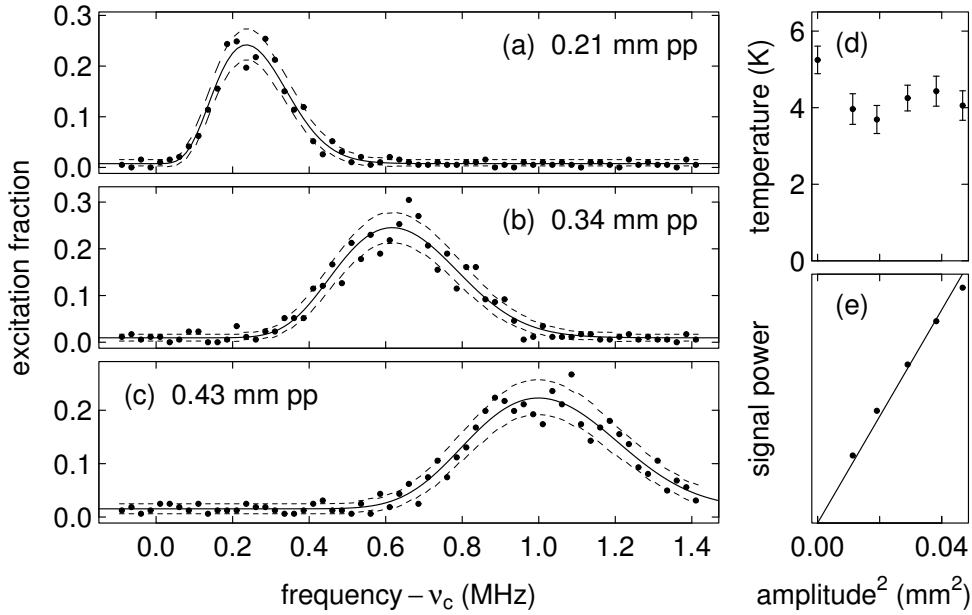
Figure 15: (a-c) Measured quantum jump spectra (points), fits to $P_c(\nu; E_o, T_z)$ (solid) and 68% confidence limits (dashes) for the comparator SEO conditions of Fig. 13a-c. (d) T_z from the fits. (e) Induced signal (in arbitrary units) is proportional to A_o^2 from fits.

ambient temperature, emphasizing that either this amplifier must be off, or feedback cooling must be applied, [5] to achieve low axial temperatures. Fig. 15e shows that the extracted $E_o \sim A_o^2$ is proportional to the induced signal power, which can be measured in only seconds. The quantum jump spectroscopy in Fig. 15 which calibrates this signal took about 40 hours.

The one-electron SEO allows such good detection of small frequency shifts that a likely application is the measurement of electron and positron magnetic moments – to provide the most accurate direct lepton CPT test, and the most accurate determination of the fine structure constant α. Figs. 14b-c illustrate the detection of a one-quantum cyclotron excitation and a spin flip. Quantum jump spectroscopy – measuring the number of quantum jumps as appropriate drive frequencies are changed – could provide the first fully quantum measurement of these moments.

Averaging the frequency of a one-antiproton ($\overline{\text{p}}$) SEO over a long time, to detect extremely small δ, may make possible the long-time goal [48] of measuring the $\overline{\text{p}}$ magnetic moment. Improving the 0.3% current accuracy [49] by a factor of a million or more seems conceivable. The needed ν_c can already be measured to such an accuracy [50]. Measuring the needed spin precession frequency requires observing a $\overline{\text{p}}$ spin flip. The δ that would signal such a flip is proportional to $\mu/\sqrt{m}$ for a particle with magnetic moment μ and mass m. The challenge is that μ for the $\overline{\text{p}}$ is 658 times smaller than that of the electron, and $\sqrt{m}$ is 43 times larger, so that δ is a daunting 3×10^4 smaller than that of an an electron in the same trap.

Fortunately, the size of the frequency shift δ can be increased, since δ is proportional to an apparatus factor $\beta M/(d\sqrt{V_o})$ [19]. For example, making the ring electrode in the trap of Fig. 11 out of iron rather than copper would increase the product of a relative geometry factor β and the magnetization M for the magnetic material (and hence δ) by a factor of 16. Substantial additional increases could come

from reducing the trap size and potential, d and V_o, limited by the extent to which this makes a more anharmonic axial oscillation. The fractional stability required in the trapping potential goes as $\mu \beta M / V_o$ and seems possible. To avoid broadened resonances, spin flips and cyclotron excitations would be made in a trap without a magnetic gradient, then transferred to a detection trap with a large magnetic gradient, as in measurements of magnetic moments of bound electrons [51].

In conclusion, self-excitation is demonstrated with the simplest of microscopic oscillators - a single electron suspended in a Penning trap. Both a comparator and a DSP are used to stabilize large, easily observed oscillations that are much larger than noise-driven fluctuations. Despite the anharmonic trap potential, with the right choice of feedback gain, the SEO rapidly excites itself to a large oscillation that is locally harmonic – with an oscillation frequency largely independent of amplitude fluctuations. It maintains the large oscillation even when its oscillation frequency shifts suddenly. The great signal-to-noise ratio observed with the SEO makes it possible to detect small frequency shifts quickly. The SEO could thus enable better measurements of the electron and positron magnetic moments. It may also make it possible to detect antiproton spin flips for the first time, thereby opening the way to greatly improved measurements of the antiproton magnetic moment.

5   New Measurement of the Electron Magnetic Moment

The discussion of a new measurement of the electron magnetic moment in this section is based a recent report [7] that was published in collaboration with my students, B. Odom, B. D'Urso and D. Hanneke.

Measurements of the electron magnetic moment ($\boldsymbol{\mu}$) probe the electron's interaction with the fluctuating vacuum of QED, and also probe for possible electron substructure. As an eigenstate of spin $\mathbf{S}$, the electron (charge $-e$ and mass m) has $\boldsymbol{\mu} \propto \mathbf{S}$,

$$\boldsymbol{\mu} = -g \frac{e\hbar}{2m} \frac{\mathbf{S}}{\hbar}. \tag{22}$$

The g-value is a dimensionless measure of the moment[1], with the dimensions and approximate size given by the Bohr magneton, $e\hbar/(2m)$. If the electron was a mechanical system with an orbital angular momentum, then g would depend upon the relative distributions of the rotating charge and mass, with $g = 1$ for identical distributions. (Cyclotron motion of a charge in a magnetic field B, at frequency $\nu_c = eB/(2\pi m)$, is one example.) A Dirac point particle has $g = 2$. QED predicts that vacuum fluctuations and polarization slightly increase this value. Electron substructure [52] would make g deviate from the Dirac/QED prediction (as quark-gluon substructure does for a proton).

Measurements of the electron g have a long history [53, 54], with a celebrated measurement [20] providing the accepted value [55] since 1987. The new g has a six times smaller standard deviation and is shifted by 1.7 standard deviations (Fig. 16a). A one-electron quantum cyclotron [4], cavity-inhibited spontaneous emission [24], a

---

[1] The "g" used here and in what follows should not be confused the feedback gain in Section 3 which unfortunately is referred to with the same symbol.

self-excited oscillator (SEO) [6], and a cylindrical Penning trap [1] contribute to the extremely small uncertainty. For the first time, spectroscopy is done with the lowest cyclotron and spin levels of a single electron fully resolved via quantum non-demolition (QND) measurements [4], and a cavity shift of g is directly observed.
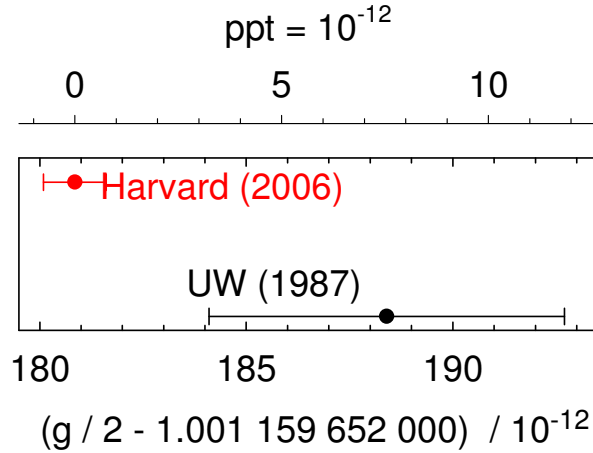

Figure 16: Measurements of the electron g-value.

What can be learned from the more accurate electron g? The first result beyond g itself is the fine structure constant, $\alpha = e^2/(4\pi\epsilon_0\hbar c)$, determined from g and QED with ten times smaller uncertainty compared to any other method [8]. This fundamental measure of the strength of the electromagnetic interaction is a crucial ingredient in our system of fundamental constants [55]. Second, the most demanding test of QED continues to be a comparison of measured and calculated g-values, and the way is now prepared for a ten times more stringent test. Third, even though muon g-values [56] have nearly 1000 times larger uncertainties compared to the electron g, heavy particles (possibly unknown in the standard model) make a contribution that is relatively much larger for the muon. However, the contribution is small compared to the calculated QED contribution which depends on α and must be subtracted out. The electron g provides α and a confidence-building test of the required QED.

The g-value determines the spin frequency $\nu_s = \frac{g}{2}\nu_c$ for a free electron in a magnetic field $B\hat{\mathbf{z}}$. To weakly confine the electron, an electric quadrupole potential, $V \sim 2z^2 - \rho^2$, is added, with $\boldsymbol{\rho} = x\hat{\mathbf{x}} + y\hat{\mathbf{y}}$. Optimal biasing of the electrodes (Fig. 17a) of an orthogonalized cylindrical Penning trap [1] minimizes an undesired z^4 term. The electron-trap system has four eigenfrequencies. The spin and trap-modified cyclotron frequencies are approximately equal at $\nu_s \approx \bar{\nu}_c \approx 149$ GHz. A harmonic axial oscillation along $\mathbf{B}$ is at $\bar{\nu}_z \approx 200$ MHz, and an orthogonal circular magnetron oscillation is at $\bar{\nu}_m \approx 134$ kHz. The latter three frequencies are shifted by the unavoidable leading imperfections of a real Penning trap – harmonic distortions of the quadrupole potential, and a misalignment of the electrode axis and $\mathbf{B}$ [57]. Silver trap electrodes were used after the nuclear paramagnetism of copper electrodes caused unacceptable temperature-dependent fluctuations in $\mathbf{B}$ near 100 mK.

The spin motion is undamped, being essentially uncoupled from its environment [19]. The cyclotron motion would damp in ~ 0.1 s via synchrotron radiation in free space. This spontaneous emission is greatly inhibited in the trap cavity (to 6.7 s or 1.4 s here) when $\mathbf{B}$ is tuned so $\bar{\nu}_c$ is far from resonance with cavity radiation
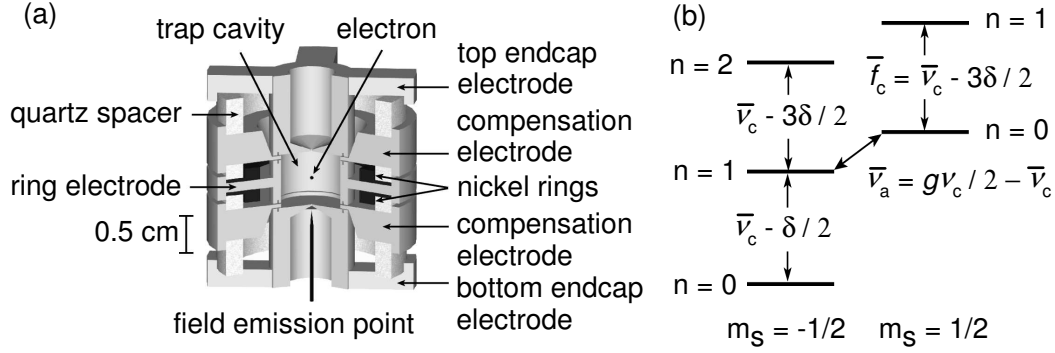
Figure 17: Cylindrical Penning trap cavity used to confine a single electron and inhibit spontaneous emission (a), and the cyclotron and spin levels of an electron confined within it (b).

modes [24, 19]. Blackbody photons that would excite the cyclotron ground state are eliminated by cooling the trap and vacuum enclosure below 100 mK with a dilution refrigerator [4]. (Thermal radiation through the microwave inlet makes < 1 excitation/hr.) The axial motion, damped by a resonant circuit, cools below 0.3 K (from 5 K) when the axial detection amplifier is off for crucial periods. The magnetron motion radius is minimized with axial sideband cooling [19].

For the first time, g is deduced from observed transitions between only the lowest of the spin ($m_s = \pm 1/2$) and cyclotron ($n = 0, 1, 2, \ldots$) energy levels (Fig. 17b),

$$E(n, m_s) = \frac{g}{2} h \nu_c m_s + (n + \tfrac{1}{2}) h \bar{\nu}_c - \tfrac{1}{2} h \delta (n + \tfrac{1}{2} + m_s)^2. \tag{23}$$

The needed $\nu_c = eB/(2\pi m)$ (for a free electron in a magnetic field) is related to the observable eigenfrequencies by the Brown-Gabrielse invariance theorem [57],

$$(\nu_c)^2 = (\bar{\nu}_c)^2 + (\bar{\nu}_z)^2 + (\bar{\nu}_m)^2, \tag{24}$$

which applies despite the mentioned imperfection shifts of the three eigenfrequencies. The third term in Eq. 23, the leading relativistic correction [19] with $\delta/\nu_c \equiv h\nu_c/(mc^2) \approx 10^{-9}$, would add uncertainty to the measurement if cyclotron energy levels were not resolved.

The anomaly and spin-up cyclotron frequencies ($\bar{\nu}_a \approx 173$ MHz and $\bar{f}_c$ in Fig. 17b) are measured, since

$$\frac{g}{2} = \frac{\bar{\nu}_c + \bar{\nu}_a}{\nu_c} \simeq 1 + \frac{\bar{\nu}_a - \bar{\nu}_z^2/(2\bar{f}_c)}{\bar{f}_c + 3\delta/2 + \bar{\nu}_z^2/(2\bar{f}_c)}. \tag{25}$$

We use the approximation to the right which requires no measurement of $\bar{\nu}_m$. It incorporates an expansion of the invariance theorem [57], using $\bar{\nu}_c \gg \bar{\nu}_z \gg \bar{\nu}_m \gg \delta$. Corrections go as the product of $(\bar{\nu}_z/\bar{\nu}_c)^4 \sim 10^{-12}$ and a misalignment/harmonic distortion factor $\sim 10^{-4}$ [57].

A change in cyclotron or spin state is revealed by $\bar{\nu}_z$ shifts (Fig. 18a-b) of a one-electron self-exited oscillator (SEO) [6]. The electron's axial oscillation induces a signal in a resonant circuit that is amplified and fed back to drive the oscillation. QND couplings of spin and cyclotron energies to $\bar{\nu}_z$ [4] arise because saturated nickel rings (Fig 17a) produce a small magnetic bottle, $\Delta \mathbf{B} = \beta_2[(z^2 - \rho^2/2)\hat{\mathbf{z}} - z\rho\hat{\boldsymbol{\rho}}]$ with $\beta_2 = 1540$ T/m^2.

Anomaly transitions are induced by applying potentials oscillating at $\bar{\nu}_a$ to electrodes, to drive an off-resonance axial motion through the bottle's $z\boldsymbol{\rho}$ gradient. The electron sees the oscillating magnetic field perpendicular to $\mathbf{B}$ as needed to flip its spin, with a gradient that allows a simultaneous cyclotron transition. Cyclotron transitions are induced by microwaves with a transverse electric field that are injected into and filtered by the cavity. The electron samples the same magnetic gradient while $\bar{\nu}_a$ and $\bar{f}_c$ transitions are driven, because both drives are kept on, with one detuned slightly so that only the other causes transitions.
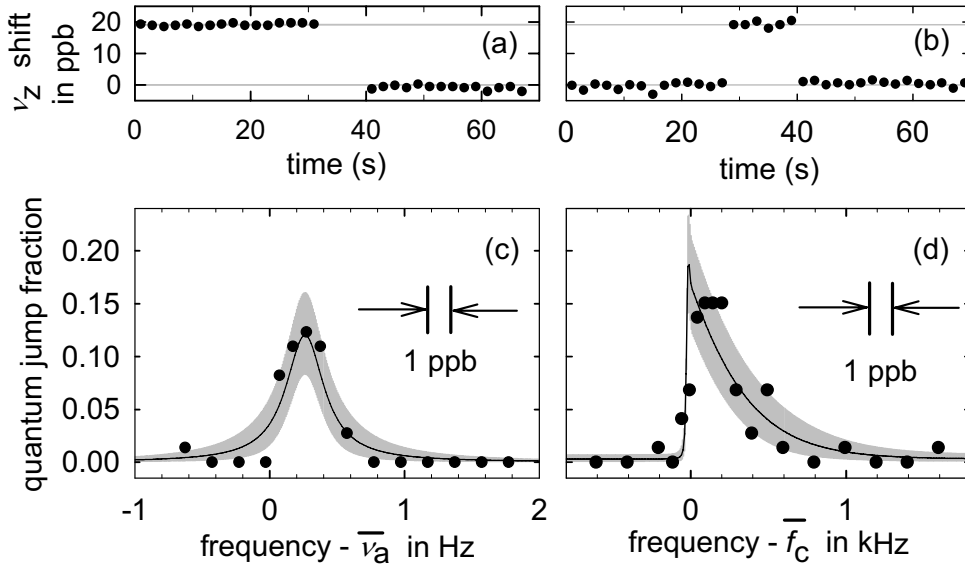

Figure 18: Sample $\bar{\nu}_z$ shifts for a spin flip (a) and for a one-quantum cyclotron excitation (b). Quantum jump spectroscopy lineshapes for anomaly (c) and cyclotron (d) transitions, with a maximum likelihood fit to the calculated lineshapes (solid). The bands indicate 68% confidence limits for distributions of measurements about the fit values.

A measurement starts with the SEO turned on to verify that the electron is in the upper of the two stable ground states, $|n = 0, m_s = 1/2\rangle$. Simultaneous $\bar{\nu}_c - \delta/2$ and $\bar{\nu}_a$ drives prepare this state as needed. The magnetron radius is reduced with 1.5 s of strong sideband cooling [19] at $\bar{\nu}_z + \bar{\nu}_m$, and the detection amplifier is turned off. After 1 s, either a $\bar{f}_c$ drive, or a $\bar{\nu}_a$ drive, is on for 2 s. The detection amplifier and the SEO are then switched on to check for a cyclotron excitation, or a spin flip (from an anomaly transition followed by a cyclotron decay). Inhibited spontaneous emission gives the time needed to observe a cyclotron excitation before an excited state decays. We step through each $\bar{\nu}_c$ and $\bar{\nu}_a$ drive frequency in turn, recording the number of quantum jumps per drive attempt. This measurement cycle is repeated during nighttimes, when electrical and magnetic noise are lower. A low drive strength keeps the transition probability below 20% to avoid saturation effects.

Quantum jump spectroscopy (measuring the quantum jumps per attempt to drive them as a function of drive frequency) gives resonance lineshapes for $\bar{f}_c$ and $\bar{\nu}_a$ (Fig. 18c-d). For weak drives that avoid saturation, the line shape comes from thermal axial motion within the magnetic bottle [46]. The small coherent axial oscillation at $\bar{\nu}_a$ has no noticeable effect. However, otherwise undetectable ppb fluctuations in

B, on time scales shorter than an hour, would smear the expected lineshapes.

At the first of two magnetic fields used, $\bar{\nu}_c \approx 146.8$ GHz. A 1.4 s damping time gives good lineshape statistics (e.g., Fig. 18c-d) with 66 measurement cycles per night on average. Three methods to extract $\bar{\nu}_a$ and $\bar{f}_c$ from lineshapes give the same g within 0.6 ppt – our "lineshape model" uncertainty in Table 1. The first is maximum likelihood fitting of the Brownian motion lineshape. The second method fits a convolution of this lineshape and a Gaussian resolution function, about 1 ppb wide. The third method weights each drive frequency by the number of quantum jumps it produces, and uses the weighted average frequencies in Eq. 25 for $\bar{\nu}_a$ and $\bar{f}_c$. (Understood shifts proportional to axial temperature, common to both frequencies, do not increase the uncertainty.) This weighted average method should account for Brownian axial motion and additional fluctuations of **B**. At our second field, where $\bar{\nu}_c \approx 149.0$ GHz, the 6.7 s damping time allows only 29 measurement cycles per night on average. A long wait is needed to make certain that a spin flip has not occurred. The weighted averages method is used for the lower statistics lineshapes.

The $\bar{\nu}_z$ in Eq. 25 pertains while $\bar{f}_c$ and $\bar{\nu}_a$ are driven – not what is measured when the SEO amplifier is on and increasing the axial temperature from 0.3 to 5 K. Limits on axial heating shifts come from the width of a notch in the noise spectrum resonance for the resonant circuit [19] (Table 1), measured less well for $\bar{\nu}_c \approx 146.8$ GHz.

Source $\bar{\nu}_c =$	146.8 GHz	149.0 GHz
$\bar{\nu}_z$ shift	0.2(0.3)	0.00(0.02)
Anomaly power	0.0(0.4)	0.00(0.14)
Cyclotron power	0.0(0.3)	0.00(0.12)
Cavity shift	12.8(5.1)	0.06(0.39)
Lineshape model	0.0 (0.6)	0.00 (0.60)
Statistics	0.0 (0.2)	0.00 (0.17)
Total (in ppt)	**13.0(5.2)**	**0.06(0.76)**

Table 1: Applied corrections and uncertainties for g in ppt.

Although the g-value from Eq. 25 is independent of **B**, field stability is still an important challenge, since $\bar{\nu}_a$ and $\bar{f}_c$ are measured at different times. After the superconducting solenoid settles for several months, field drifts below 10^{-9}/night have been observed. This requires regulating five He and N_2 pressures in the solenoid and experiment cryostats, and the surrounding air temperature to 0.3 K. We correct for drifts up to 10^{-9}/hr using a cyclotron resonance edge measured once in three hours.

The trap cavity modifies the density of states of radiation modes of free space, though not enough to significantly affect QED calculations of g [58]. However, cavity radiation modes do shift $\bar{f}_c$ [3] – still a significant uncertainty, as in the past [3, 20]. We use a synchronized-trapped-electrons method [17] to observe quantitatively understandable radiation modes (Fig. 19a) of a good cylindrical Penning trap cavity [1]. Our best measurement comes from choosing $\bar{\nu}_c \approx 149.0$ GHz, maximally detuned from modes that couple to a centered electron's cyclotron motion. A measurement at $\bar{\nu}_c \approx 146.8$ GHz, uncomfortably close to TE_{127}, checks how well cavity shifts are understood. Until the cavity spectrum and its frequency calibration is more carefully studied, TE_{127} and TM_{143} are assumed only to lie within the shaded bands. A renormalized calculation (Eq. 8.19 of [19]) gives a range of possible cavity shifts

of the measured g (Fig. 19b) that is insensitive to mode quality factors for $Q > 500$. Assigned shifts and uncertainties are indicated in Fig. 19b and in Table 1. The first direct observation of a cavity shift of g, the difference between our two measurements (Fig. 19c), lies within the predicted range.
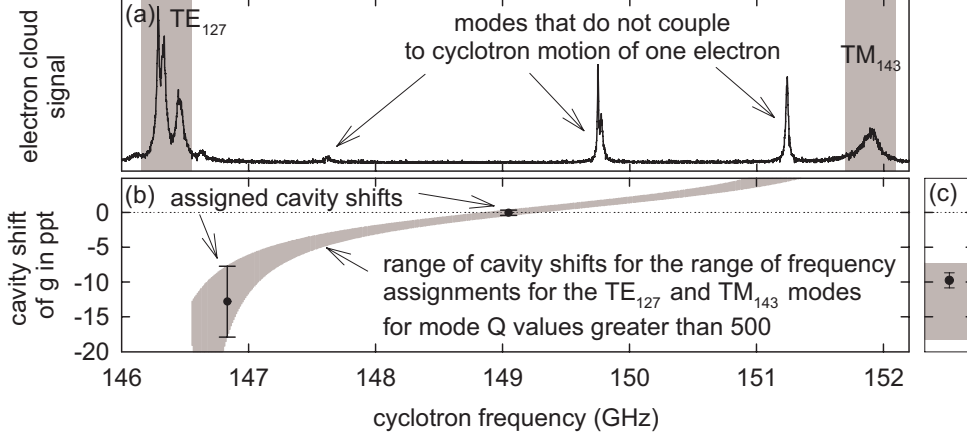

Figure 19: Modes of the trap cavity observed with synchronized electrons (a). Resulting assigned cavity shifts (points and Table 1) (b). First measured cavity shift of g (point) is the shift between measurements at 146.8 and 149.0 GHz (c). Gray bands are the assumed calibration and identification uncertainties for mode frequencies in (a), and the resulting range of predicted cavity shifts in (b) and (c).

A new value for the electron magnetic moment,

$$g/2 = 1.001\,159\,652\,180\,85\,(76) \qquad (0.76\text{ ppt}), \tag{26}$$

comes from the measurement at $\bar{\nu}_c \approx 149.0$ GHz. (A weighted average with the more uncertain measurement at $\bar{\nu}_c \approx 146.8$ GHz is larger by 0.06 ppt, with a decreased uncertainty of 0.75 ppt.) The standard deviation, about six times smaller than from any previous measurement, arises mostly from the lineshape model and cavity shifts (Table 1). Varying the $\bar{\nu}_a$ and $\bar{f}_c$ drive power causes no detectable shifts of g.

QED provides an asymptotic series relating g and α,

$$\frac{g}{2} = 1 \;+\; C_2\left(\frac{\alpha}{\pi}\right) + C_4\left(\frac{\alpha}{\pi}\right)^2 + C_6\left(\frac{\alpha}{\pi}\right)^3 + C_8\left(\frac{\alpha}{\pi}\right)^4$$
$$+ \;\; ... + a_{\mu\tau} + a_{\text{hadronic}} + a_{\text{weak}}, \tag{27}$$

with hadronic and weak contributions added, and assuming no electron substructure. Impressive calculations, summarized in the next section, give exact C_2, C_4 and C_6, a numerical value and uncertainty for C_8, and a small $a_{\mu\tau}$.

The next section details a new determination of α, from the measured g and Eq. 27,

$$\alpha^{-1}(\text{H06}) \;=\; 137.035\,999\,070\,(12)\,(37)\,(90) \tag{28}$$
$$=\; 137.035\,999\,070\,(98) \quad [0.71\text{ ppb}], \tag{29}$$

The first line gives the experimental uncertainty first and the QED uncertainty second, including an estimated contribution from a yet uncalculated C_{10} [8]. The total 0.70 ppb uncertainty is ten times smaller than for the next most precise methods

(Fig. 16b) – determining α from measured mass ratios, optical frequencies, together with either Rb [59] or Cs [60] recoil velocities.

The most stringent test of QED (one of the most demanding comparisons of any calculation and experiment) continues to come from comparing measured and calculated g-values, the latter using an independently measured α as an input. The next section shows that the new g, compared to Eq. 27 with $\alpha(\text{Cs})$ or $\alpha(\text{Rb})$, gives a difference $|\delta g/2| < 17 \times 10^{-12}$. The small uncertainties in $g/2$ will allow a ten times more demanding test if ever the large uncertainties in the independent α values can be reduced. The prototype of modern physics theories is thus tested far more stringently than its inventors ever envisioned [61], with better tests to come.

The same comparison of theory and experiment probes the internal structure of the electron [8, 52] – limiting the electron to constituents with a mass $m^* > m/\sqrt{\delta g/2} = 130 \text{ GeV}/\text{c}^2$, corresponding to an electron radius $R < 1 \times 10^{-18}$ m. If this test was limited only by our experimental uncertainty in g, then we could set a limit $m^* > 600$ GeV. These high energy limits seem somewhat remarkable for an experiment carried out at 100 mK.

Are experimental improvements possible? A reduction of the 0.76 ppt uncertainty of the measured electron g seems likely, given that this fully-quantum measurement has only recently been realized. Time is needed to study the lineshapes and cavity shifts as a function of magnetic field, to improve cooling methods, and to make the magnetic field more stable.

In conclusion, greatly improved measurements of the electron magnetic moment and the fine structure constant, and a sensitive probe for internal electron structure, come from resolving the lowest cyclotron and spin levels of a one-electron quantum cyclotron. A self-excited oscillation of the electron reveals one-quantum transitions. A cylindrical Penning trap cavity narrows resonance lines by inhibiting spontaneous emission. Electromagnetic modes of this understandable cavity geometry, probed with synchronized electrons, shift g in a measurable way that can be corrected. The new $g/2$ differs from a long accepted value by 1.7 standard deviations, and its fractional uncertainty of 7.6×10^{-13} is nearly six times smaller. The new α has an uncertainty ten times smaller than that from any other method to determine the fine structure constant.

6   New Determination of the Fine Structure Constant

The new determination of the fine structure constant discussed in this section was initially reported in collaboration with my students D. Hanneke and B. Odom, and in collaboration with theorists T. Kinoshita and M. Nio [8]. This section has been updated to include the most recent correction to the QED evaluation [9].

The electron g-value, the dimensionless measure of the electron magnetic moment in terms of the Bohr magneton, provides our most sensitive probe into the structure of what is believed to be the only stable point particle with substantial mass – a particle that seems very insensitive to physics at small distance scales. The fundamental fine structure constant, $\alpha = e^2/(4\pi\epsilon_0\hbar c)$, gives the strength of the elec-

tromagnetic interaction, and is a crucial building block in our system of fundamental constants [55]. Quantum electrodynamics (QED), the wonderfully successful theory that describes the interaction of light and matter, provides an incredibly accurate prediction for the relationship between g and α, with only small corrections for short distance physics.

A new measurement of g [7] achieves an accuracy that is nearly six times more accurate than the last measurement of g back in 1987 [20]. An improved QED calculation that includes contributions from 891 Feynman diagrams [62] now predicts g in terms of α through order $(\alpha/\pi)^4$. Together, the newly measured g, with the more accurate QED calculation, determined a new and much more accurate determination of α. It is the first higher accuracy measurement of α since 1987 (Fig. 20), and is ten times more accurate than any other method to determine α. The most stringent test of QED is also presented.
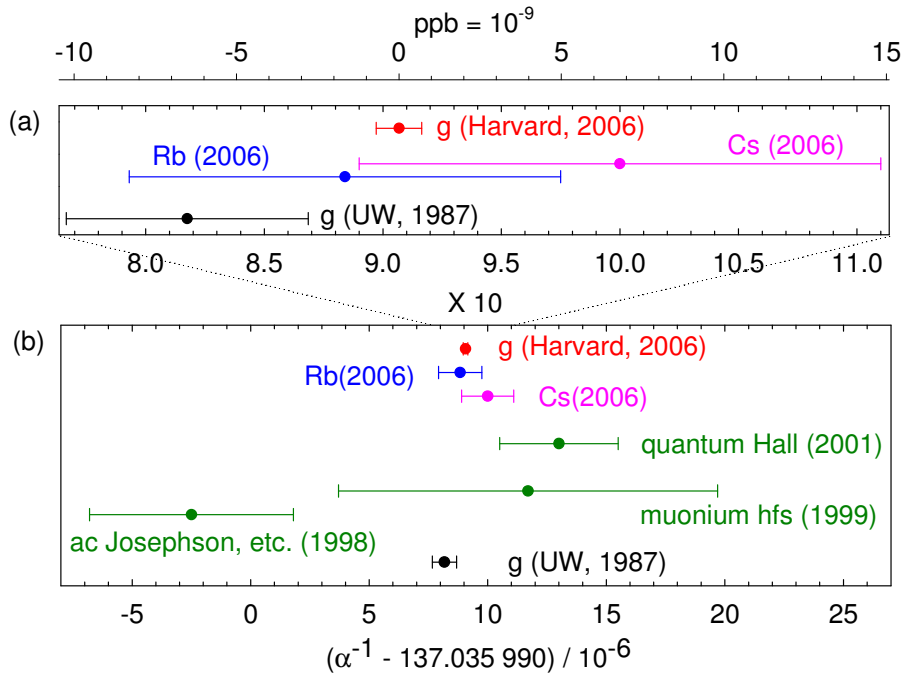

Figure 20: A ten times expanded scale (a) is required to see the small uncertainties in the new α announced here. Traditional determinations can be seen on a larger scale (b). Measured g are converted to α using current QED theory.

Since $g = 2$ for a Dirac point particle, the dimensionless moment is often written as $g = 2(1 + a)$. The deviation a has come to be called the anomalous magnetic moment of the electron or sometimes simply the electron anomaly. It arises almost entirely from the vacuum fluctuations and polarizations that are described by QED,

$$a = a(QED) + a(hadron) + a(weak), \qquad (30)$$

with only small additions for short distance physics, well understood in the context of the standard model [63] (unlike the case for the heavier muon lepton). Any additional contribution to the anomaly would therefore be extremely significant, indicating electron substructure [52], new short distance physics, or problems with QED theory (and perhaps with quantum field theory more generally).

A long tradition of improved measurements of g [53, 20] now continues after a hiatus of nearly twenty years. A new measurement achieves a much higher accuracy for g [7] by resolving the quantum cyclotron and spin levels of one electron suspended for months at a time in a cylindrical Penning trap. Quantum jump spectroscopy of transitions between these levels determines the spin and cyclotron frequencies, and $g/2$ is essentially the ratio of such measured frequencies. The cylindrical Penning cavity shapes the radiation field in which the electron is located, narrowing resonance linewidths by inhibiting spontaneous emission, and providing boundary conditions which make it possible to identify the symmetries of cavity radiation modes. A QND (quantum nondemolition) coupling, of the cyclotron and spin energies to the frequency of an orthogonal and nearly harmonic electron oscillation, reveals the quantum state. This harmonic oscillation of the electron is self-excited, by a signal derived from its own motion, to produce the large signal-to-noise ratio needed to quickly read out the quantum state without ambiguity.

The newly measured g has an uncertainty of only 7.6 parts in 10^{13}. Subtracting off the $g = 2$ for a Dirac point particle gives an anomaly [7]

$$a(\text{H06}) = 1\,159\,652\,180.85\,(76) \times 10^{-12} \quad [0.66 \text{ ppb}]. \tag{31}$$

As detailed in the previous section, the uncertainty mostly originates from three sources. The largest contribution arises from imperfect fits to the expected lineshape model; likely these can be understood and reduced with careful study. Tiny magnetic field instabilities are one possible cause. The second source of uncertainty is cavity shifts, caused when the cyclotron frequency of an electron in trap cavity is shifted by interactions with cavity radiation modes that are near in frequency. The frequencies of cavity radiation modes are measured well enough to identify the spatial symmetry of the modes, and to calculate and correct for cavity shifts to g from the known electromagnetic field configurations. A smaller third uncertainty is statistical, and could be reduced as needed with more measurements.

QED calculations involving many Feynman diagrams provide the coefficients for expansions in powers of the small ratio $\alpha/\pi \approx 2 \times 10^{-3}$. The QED anomaly

$$\begin{aligned} a(\text{QED}) &= A_1 + A_2(m_e/m_\mu) + A_2(m_e/m_\tau) \\ &+ A_3(m_e/m_\mu, m_e/m_\tau), \end{aligned} \tag{32}$$

is a function of lepton mass ratios. Each A_i is a series,

$$A_i = A_i^{(2)} \left(\frac{\alpha}{\pi}\right) + A_i^{(4)} \left(\frac{\alpha}{\pi}\right)^2 + A_i^{(6)} \left(\frac{\alpha}{\pi}\right)^3 + \dots. \tag{33}$$

The calculations are so elaborate that isolating and eliminating mistakes is a substantial challenge, as is determining and propagating numerical integration uncertainties.

Fig. 21 compares the contributions and uncertainties for $g/2$. The leading constants for second [64], third [65, 66, 67] and fourth [68, 69, 70, 71, 72] orders,

$$A_1^{(2)} = 0.5, \tag{34}$$

$$A_1^{(4)} = -0.328\,478\,965\,579\,\dots, \tag{35}$$

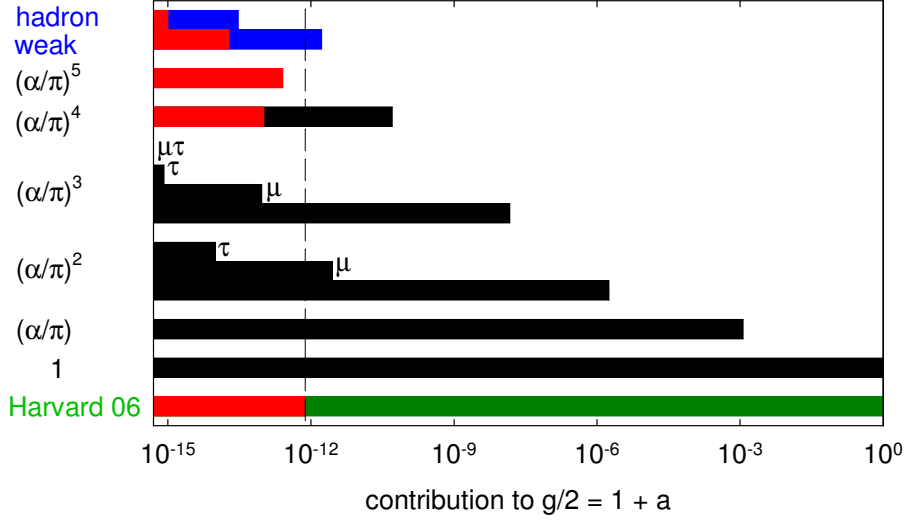$$A_1^{(6)} = 1.181\,241\,456\,\dots, \tag{36}$$

Figure 21: Contributions to $g/2$ for the experiment (green), terms in the QED series (black), and from small distance physics (blue). Uncertainties are in red. The μ, τ and $\mu\tau$ indicate terms dependent on mass ratios m_e/m_μ, m_e/m_τ and the two ratios, m_e/m_μ and m_e/m_τ, respectively.

have been evaluated exactly. The latter confirms the value $1.181\,259\,(4)$ obtained numerically [73]. Mass-dependent QED additions [74, 75, 76, 77, 78, 79],

$$
\begin{aligned}
A_2^{(4)}(m_e/m_\mu) &= 5.197\,386\,70\,(27) \times 10^{-7}, \\
A_2^{(4)}(m_e/m_\tau) &= 1.837\,63\,(60) \times 10^{-9}, \\
A_2^{(6)}(m_e/m_\mu) &= -7.373\,941\,58\,(28) \times 10^{-6}, \\
A_2^{(6)}(m_e/m_\tau) &= -6.581\,9\,(19) \times 10^{-8}, \\
A_3^{(6)}(m_e/m_\mu, m_e/m_\tau) & \\
&= 0.190\,95\,(63) \times 10^{-12},
\end{aligned}
\tag{37}
$$

make only very small contributions. Uncertainties derive from the uncertainties in measured lepton mass ratios.

Crucial progress came in evaluating, checking, and determining the uncertainty in the eighth order $A_1^{(8)}$, which includes contributions of 891 Feynman diagrams. Typical diagrams of the 13 gauge invariant subgroups are shown in Fig. 22. Integrals of 373 of these (Groups I - IV) have been verified (and corrected) by more than one independent formulation [80, 62]. The 518 diagrams of Group V, with no closed lepton loops, await completion of an independent verification. However, their renormalization terms are derived by systematic reduction of original integrands applying a simple power-counting rule [81], allowing extensive cross-checking among themselves and with exactly known diagrams of lower order [82]. Numerical integrations with VEGAS [83], on many supercomputers over more than 10 years [62, 84], then yields

$$
A_1^{(8)} = -1.9144\,(35)
\tag{38}
$$

The uncertainty, determined using estimated errors from VEGAS, is improved by an order of magnitude over the previous value [85].

This value differs from that listed in [8]. An automated code generator [62], produced to calculate the tenth-order contribution to $g/2$, was used to examine the

518 of 891 eighth-order QED diagrams that had no previous independent check. Only 47 integrals represent the 518 vertex diagrams when the Ward-Takahashi identity and time-reversal invariance are used. A diagram-by-diagram comparison with the previous calculation [86] showed that 2 of the 47 require a corrected treatment of infrared divergences [84], leading to the corrected value used here.

Is it likely that other adjustments of the QED theory will shift the α that is determined from the electron g? Hopefully not, now that all eighth-order contributions have been checked independently by two or more methods for the first time. What could further shift this determination of α would be a larger-than-expected tenth-order QED contribution to g/2 – now being evaluated using the new computational method that revealed the need for this update.

The summary of precise α determinations (Fig. 20) differs from that of one year earlier [8] in several ways. The corrected QED evaluation shifts the α from the Harvard and UW g measurements. The atom-recoil determination of α(Rb) shifts due to an experimental correction [87]. The neutron α is no longer included awaiting a change required by the reevaluations of the Si lattice constant and its uncertainties (eg. [88]).
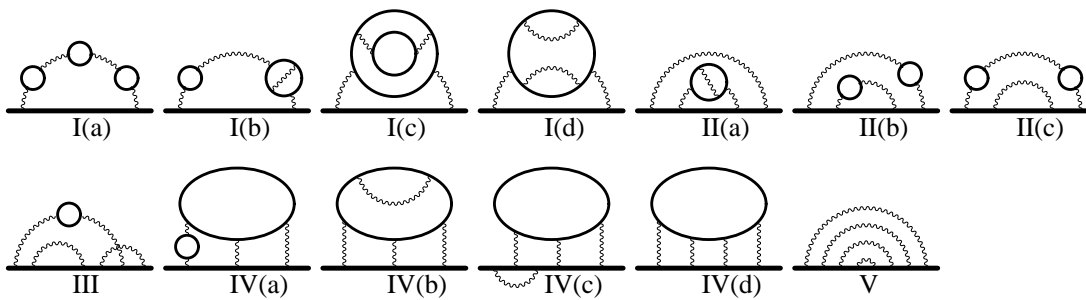

Figure 22: Typical diagrams from each gauge invariant subgroup that contributes to the eighth-order electron magnetic moment. Solid and wiggly curves represent the electron and photon, respectively. Solid horizontal lines represent the electron in an external magnetic field.

The high experimental precision makes the tenth order contribution to g potentially important if the unknown $A_1^{(10)}$ is unexpectedly large, though this seems unlikely. To get a feeling for its possible impact we use a bound

$$|A_1^{(10)}| < x \tag{39}$$

with an estimate $x = 4.6$ [55], while awaiting a daunting evaluation of contributions from 12672 Feynman diagrams that is now underway [62].

Also owing the high precision, non-QED contributions,

$$\begin{aligned} a(\text{hadron}) &= 1.682\,(20) \times 10^{-12}, \\ a(\text{weak}) &= 0.030\,(01) \times 10^{-12}, \end{aligned} \tag{40}$$

must be included. Fortunately, these are small and well understood in the context of the standard model [55, 63]. They are much larger and more important for the muon.

The new experimental measurement of g, and the greatly improved QED calculation, thus determine a value of α that is ten times more accurate than any other

method to determine α,

$$
\begin{aligned}
\alpha^{-1}(\text{H06}) &= 137.035\,999\,070\,(12)\,(37)\,(90) & (41)\\
&= 137.035\,999\,070\,(98) \quad [0.71\ \text{ppb}], & (42)
\end{aligned}
$$

In the first line, the first uncertainty is from the calculated $A_1^{(8)}$ and the last is from the measured g. The middle uncertainty is from the estimated bound on the unknown $A_1^{(10)}$ in Eq. (39). More generally it is $(8x)$, which rounds to (37) for the estimate $x = 4.6$ [55].

Note that while the tenth order impact on α is not large since $8x \ll 90$, a real calculation will be needed before a much more accurate α can be deduced from a better g. Note also that the exact $A_1^{(6)}$ of Laporta and Remiddi, in Eq. (36) and [72], eliminates an earlier numerical uncertainty [73] that would add (60) to the list of three uncertainties in Eq. (41), significantly increasing the total uncertainty in Eq. (42).

Testing QED requires an independent measurement of α, to be used with QED theory, to determine an anomaly that can be compared to what is measured. Recent measurements utilizing Cs and Rb atoms yield

$$
\begin{aligned}
\alpha^{-1}(Cs06) &= 137.036\,000\,00\,(110) & [8.0\ \text{ppb}], & (43)\\
\alpha^{-1}(Rb06) &= 137.035\,998\,84\,(\,91) & [6.6\ \text{ppb}]. & (44)
\end{aligned}
$$

The latest versions rely upon many experiments, including the measured Rydberg constant [89], the Cs or Rb mass in amu [90], and the electron mass in amu [91, 92]. The needed $\hbar/M[Cs]$ comes from an optical measurement of the Cs D1 line [60, 93], and the "preliminary" recoil shift for a Cs atom in an atom interferometer [94]. The needed $\hbar/M[Rb]$ come from a measurement of an atom recoil of a Rb atom in an optical lattice [59] as recently corrected[87].

The Cs and Rb determinations of α, together with QED theory (and hadronic and weak corrections), give

$$
\begin{aligned}
a(Cs06) &= 1\,159\,652\,173.00\,(0.10)\,(0.31)\,(9.30) \times 10^{-12},\\
a(Rb06) &= 1\,159\,652\,182.80\,(0.10)\,(0.31)\,(7.70) \times 10^{-12}.
\end{aligned}
$$

Uncertainties are from the eighth order calculation, the estimated tenth order limit, and the determinations of α. Calculated and measured anomalies differ by

$$
\begin{aligned}
a(\text{Cs06}) - a(\text{H06}) &= -\ 7.9\,(9.3) \times 10^{-12}, & (45)\\
a(\text{Rb06}) - a(\text{H06}) &= \ 1.9\,(7.7) \times 10^{-12}, & (46)
\end{aligned}
$$

with the uncertainties limited by the uncertainties in $\alpha(Cs)$ and $\alpha(Rb)$, in Eqs. (43)-(44).

What theory improvements might be expected in the future? The theory contribution to the uncertainty in the new α is less than that from experiment by a factor of 3. The eighth order uncertainty in $A_1^{(8)}$ can be reduced with the accumulation of better statistics in the numerical evaluation of integrals. Ambitious efforts underway aim for an analytic evaluation of this coefficient [95]. Another big theory challenge is in evaluating the tenth-order coefficient, $A_1^{(10)}$, with the mentioned contributions from 12672 Feynman diagrams. Work underway suggests that it should be possible

to evaluate $A_1^{(10)}$ to a few percent, reducing the theoretical uncertainty in a_e to 0.1 ppb or less.

What experimental improvements can be expected? A reduction of the 0.76 ppt uncertainty of the measured electron g seems likely, given that this fully quantum measurement has only recently been realized. With time to study the lineshapes and cavity shifts at many values of the magnetic field, to improve cooling methods, and to incorporate a more stable magnetic field, an improved α from g and QED seems quite possible. Experiments are also underway under the assumption that a substantially higher accuracy can be achieved in atom recoil measurements – currently the weak link in determinations of α that are independent of g and QED. A ten-fold improved accuracy in the independent α would allow a QED test that is more stringent than current tests by this factor, even without improved measurement of g, or more accurate QED theory.

In conclusion, a slightly shifted and much more accurate determination of the fine structure constant comes from the new measurement of the electron g value, and improved QED theory. It is more accurate than any other method to determine α by a factor of ten. The working assumption is that the electron has no internal structure that is not described by QED, nor by small distance scale physics other than what is well understood within the context of the standard model of particle physics. Comparing the α from g and QED, to the α determined with Cs and Rb atoms, shows that QED continues to be a superb description of the interaction of atoms and light. However, a ten times more stringent QED test awaits a determination of α that is independent of the electron g and QED, but achieves the accuracy in the α reported here. We expect more accurate measurements of the electron g, along with more accurate QED calculations, and are thus optimistic that more accurate future determinations of α may be possible.

7   Almost Outdated

As these notes are being prepared for publication, my student D. Hanneke and I are nearly finished with our analysis of new measurements of the electron magnetic moment and the fine structure constant that look to have a precision that is two to three time better than what is reported here. Stay tuned.

8   Conclusion

Quantum jump spectroscopy of the lowest spin and cyclotron energy levels of a one-electron quantum cyclotron yields the most precise measurement of the electron magnetic moment, and the most precise measurement of the fine structure constant. The electron is suspended for months at a time in a cylindrical Penning trap, the electrodes of which provide the electrostatic quadrupole potential for trapping the

electron, and also modify the radiation field and density of states as needed to inhibit the spontaneous emission of synchrotron radiation. Feedback methods provide cooling possibilities and turn the electron into a one-particle self-excited oscillator that is used for QND measurements of the cyclotron and spin states. One spin-off measurement being pursued, in collaboration with my student S. Fogwell, is making the most stringent test of CPT invariance with a lepton system, by comparing measured g values for the electron and positron. Another spin-off measurement underway, in collaboration with my student N. Guise, is to make a one-antiproton self-excited oscillator to measure the antiprotons magnetic moment a million times more accurately than has been possible so far. A third spin-off measurement being contemplated is a direct measurement of the electron-to-proton mass ratio.

References

[1] G. Gabrielse and F. C. MacKintosh, Intl. J. of Mass Spec. and Ion Proc. **57**, 1 (1984).

[2] J. N. Tan and G. Gabrielse, Appl. Phys. Lett. **55**, 2144 (1989).

[3] L. S. Brown, G. Gabrielse, K. Helmerson, and J. Tan, Phys. Rev. Lett. **55**, 44 (1985).

[4] S. Peil and G. Gabrielse, Phys. Rev. Lett. **83**, 1287 (1999).

[5] B. D'Urso, B. Odom, and G. Gabrielse, Phys. Rev. Lett. **90**, 43001 (2003).

[6] B. D'Urso, R. Van Handel, B. Odom, D. Hanneke, and G. Gabrielse, Phys. Rev. Lett. **94**, 113002 (2005).

[7] B. Odom, D. Hanneke, B. D'Urso, and G. Gabrielse, Phys. Rev. Lett. **97**, 030801 (2006).

[8] G. Gabrielse, D. Hanneke, T. Kinoshita, M. Nio, and B. Odom, Phys. Rev. Lett. **97**, 030802 (2006).

[9] G. Gabrielse, D. Hanneke, T. Kinoshita, M. Nio, and B. Odom, Phys. Rev. Lett. **99**, 039902 (2007).

[10] X. Maître, E. Hagley, G. Nogues, C. Wunderlich, P. Goy, M. Brune, J. M. Raimond, and S. Haroche, Phys. Rev. Lett. **79**, 769 (1997).

[11] M. Weidinger, B. T. H. Varcoe, R. Heerlein, and H. Walther, in *Abstracts of ICAP 16* (Univ. of Windsor, Windsor, 1998), p. 362.

[12] P. Domokos, M. Brune, J. M. Raimond, and S. Haroche, Eur. Phys. J. D **1**, 1 (1998).

[13] D. M. Meekhof, C. Monroe, B. E. King, W. M. Itano, and D. J. Wineland, Phys. Rev. Lett. **76**, 1796 (1996).

[14] I. Bouchoule, H. Perrin, A. Kuhn, M. Morinaga, and C. Salomon, Phys. Rev. A **59**, R8 (1999).

[15] S. Gleyzes, et al, Nature **446**, 297 (2007)

[16] C. Guerlin, et al, Nature **448**, 889 (2007).

[17] J. Tan and G. Gabrielse, Phys. Rev. Lett. **67**, 3090 (1991).

[18] G. Gabrielse and J. N. Tan, *"One Electron in a Cavity"* (Academic Press, New York, 1994), pp. 267–299.

[19] L. S. Brown and G. Gabrielse, Rev. Mod. Phys. **58**, 233 (1986).

[20] R. S. Van Dyck, Jr., P. B. Schwinberg, and H. G. Dehmelt, Phys. Rev. Lett. **59**, 26 (1987).

[21] K. S. Thorne, R. W. P. Drever, and C. M. Caves, Phys. Rev. Lett. **40**, 667 (1978).

[22] V. B. Braginsky and F. Y. Khalili, Rev. Mod. Phys. **68**, 1 (1996).

[23] M. Rigo, G. Alber, F. Mota-Furtado, and P. F. O'Mahony, Phys. Rev. A **55**, 1665 (1997).

[24] G. Gabrielse and H. Dehmelt, Phys. Rev. Lett. **55**, 67 (1985).

[25] M. Strutt and A. V. der Ziel, Physica **IX**, 513 (1942).

[26] C. Kittel, '*"Elementary Statistical Physics"* (Wiley, New York, 1958), pp. 141–156.

[27] B. B. V. I. J. M. W. Milatz, J. J. Van Zolingen, Physica **19**, 195 (1953).

[28] P. G. Roll, R. Krotkov, and R. H. Dicke, Ann. of Phys. **26**, 442 (1964).

[29] R. L. Forward, J. Appl. Phys. **50**, 1 (1979).

[30] B. E. Bernard and R. C. Ritter, J. Appl. Phys. **64**, 2833 (1988).

[31] P. F. Cohadon, A. Heidmann, and M. Pinard, Phys. Rev. Lett. **83**, 3174 (1999).

[32] S. van der Meer, Rev. Mod. Phys. **57**, 689 (1985).

[33] H. Dehmelt, W. Nagourney, and J. Sandberg, Proc. Natl. Acad. Sci. USA **83**, 5761 (1986).

[34] S. L. Rolston and G. Gabrielse, Hyper. Int. **44**, 233 (1988).

[35] N. Beverini, V. Lagomarsino, G. Manuzio, F. Scuri, G. Testera, and G. Torelli, Phys. Rev. A **38**, 107 (1988).

[36] J.-M. Courty, F. Grassia, and S. Reynaud, arXiv:quant-ph/0110021 (2001).

[37] J. B. Johnson, Phys. Rev. **32**, 97 (1928).

[38] H. Nyquist, Phys. Rev. **32**, 110 (1928).

[39] S. Rainville, M. Bradley, J. Porto, J. Thompson, and D. Pritchard, Hyperfine Int. **132**, 177 (2001).

[40] A. Bain, *patent no. 8783*, Great Britain (1841).

[41] T. R. Albrecht, P. Grütter, D. Horne, and D. Rugar, J. Appl. Phys. **69**, 668 (1991).

[42] A. N. Cleland and M. L. Roukes, Nature **392**, 160 (1998).

[43] M. Lax, Phys. Rev. **160**, 290 (1967).

[44] W. B. Davenport, Jr., J. Appl. Phys. **24**, 720 (1953).

[45] W. F. Walker, T. K. Sarkar, F. I. Tseng, and D. D. Weiner, IEEE Trans. Inst. Meas. **31**, 239 (1982).

[46] L. S. Brown, Ann. Phys. (N.Y.) **159**, 62 (1985).

[47] R. S. Van Dyck, Jr., P. B. Schwinberg, and H. G. Dehmelt, Phys. Rev. Lett. **38**, 310 (1977).

[48] W. Quint and G. Gabrielse, Hyperfine Interact. **76**, 379 (1993).

[49] S. Eidelman, et al., Phys. Lett. B **592**, 1 (2004).

[50] G. Gabrielse, A. Khabbaz, D. S. Hall, C. Heimann, H. Kalinowsky, and W. Jhe, Phys. Rev. Lett. **82**, 3198 (1999).

[51] H. Häffner, T. Beier, N. Hermanspahn, H.-J. Kluge, W. Quint, S. Stahl, J. Verdú, and G. Werth, Phys. Rev. Lett. **85**, 5308 (2000).

[52] S. J. Brodsky and S. D. Drell, Phys. Rev. D **22**, 2236 (1980).

[53] A. Rich and J. C. Wesley, Rev. Mod. Phys. **44**, 250 (1972).

[54] R. S. Van Dyck Jr. , P. B. Schwinberg, and H. G. Dehmelt, *The Electron* (Kluwer Academic Publishers, Netherlands, 1991).

[55] P. J. Mohr and B. N. Taylor, Rev. Mod. Phys. **77**, 1 (2005).

[56] G. W. Bennett and et al., Phys. Rev. D **73**, 072003 (2006).

[57] L. S. Brown and G. Gabrielse, Phys. Rev. A **25**, 2423 (1982).

[58] D. G. Boulware, L. S. Brown, and T. Lee, Phys. Rev. D **32**, 729 (1985).

[59] P. Cladé, E. de Mirandes, M. Cadoret, S. Guellati-Khélifa, C. Schwob, F. Nez, L. Julien, and F. Biraben, Phys. Rev. Lett. **96**, 033001 (2006a).

[60] V. Gerginov, K. Calkins, C. E. Tanner, J. McFerran, S. Diddams, A. Bartels, and L. Hollberg, Phys. Rev. A **73**, 032504 (2006).

[61] F. Dyson, private communication.

[62] T. Aoyama, M. Hayakawa, T. Kinoshita, and M. Nio, Nucl. Phys. **B740**, 138 (2006a).

[63] A. Czarnecki, B. Krause, and W. J. Marciano, Phys. Rev. Lett. **76**, 3267 (1996).

[64] J. Schwinger, Phys. Rev. **73**, 416L (1948).

[65] C. M. Sommerfield, Phys. Rev. **107**, 328 (1957).

[66] C. M. Sommerfield, Ann. Phys. (N.Y.) **5**, 26 (1958).

[67] A. Petermann, Helv. Phys. Acta **30**, 407 (1957).

[68] S. Laporta and E. Remiddi, Phys. Lett. B **265**, 182 (1991).

[69] S. Laporta, Phys. Rev. D **47**, 4793 (1993a).

[70] S. Laporta and E. Remiddi, Phys. Lett. B **356**, 390 (1995).

[71] S. Laporta, Phys. Lett. B **343**, 421 (1995).

[72] S. Laporta and E. Remiddi, Phys. Lett. B **379**, 283 (1996).

[73] T. Kinoshita, Phys. Rev. Lett. **75**, 4728 (1995).

[74] M. A. Samuel and G. Li, Phys. Rev. D **44**, 3935 (1991).

[75] G. Li, R. Mendel, and M. A. Samuel, Phys. Rev. D **47**, 1723 (1993).

[76] A. Czarnecki and M.Skrzypek, Phys. Lett. B **449**, 354 (1999).

[77] S. Laporta, Nuovo Cim. A **106A**, 675 (1993b).

[78] S. Laporta and E. Remiddi, Phys. Lett. B **301**, 440 (1993).

[79] B. Lautrup, Phys. Lett. **69B**, 109 (1977).

[80] T. Kinoshita and M. Nio, Phys. Rev. Lett. **90**, 021803 (2003).

[81] P. Cvitanovic and T. Kinoshita, Phys. Rev. D **10**, 4007 (1974).

[82] T. Kinoshita, *Theory of the Anomalous Magnetic Moment of the Electron − Numerical Approach* (World Scientific, Singapore, 1990).

[83] G. P. Lepage, J. Comput. Phys. **27**, 192 (1978).

[84] T. Aoyama, M. Hayakawa, T. Kinoshita, and M. Nio, hep-ph/0706.3496 (2007).

[85] V. W. Hughes and T. Kinoshita, Rev. Mod. Phys. **71**, S133 (1999).

[86] T. Aoyama, M. Hayakawa, T. Kinoshita, and M. Nio, Phys. Rev. D **73**, 013003 (2006b).

[87] P. Cladé, E. de Mirandes, M. Cadoret, S. Guellati-Khélifa, C. Schwob, F. Nez, L. Julien, and F. Biraben, Phys. Rev. A **74**, 052109 (2006b).

[88] P. Becker, G. Cavagnero, U. Kuetgens, G. Mana, and E. Massa, IEEE T. on Instrum. Meas. **56**, 230 (2007).

[89] C. Schwob, L. Jozefowski, B. de Beauvoir, L. Hilico, F. Nez, L. Julien, F. Biraben, O. Acef, J. J. Zondy, and A. Clairon, Phys. Rev. Lett. **82**, 4960 (1999).

[90] M. P. Bradley, J. V. Porto, S. Rainville, J. K. Thompson, and D. E. Pritchard, Phys. Rev. Lett. **83**, 4510 (1999).

[91] T. Beier, H. Häffner, N. Hermanspahn, S. G. Karshenboim, H.-J. Kluge, W. Quint, S. Stahl, J. Verdú, and G. Werth, Phys. Rev. Lett. **88**, 011603 (2002).

[92] D. L. Farnham, R. S. Van Dyck, Jr., and P. B. Schwinberg, Phys. Rev. Lett. **75**, 3598 (1995).

[93] T. Udem, J. Reichert, R. Holzwarth, and T. W. Hänsch, Phys. Rev. Lett. **82**, 3568 (1999).

[94] A. Wicht, J. M. Hensley, E. Sarajlic, and S. Chu, Phys. Scr. **T102**, 82 (2002).

[95] S. Laporta and E. Remiddi, private communication.